



# Efficient FeCoNiCuPd thin-film electrocatalyst for alkaline oxygen and hydrogen evolution reactions

Shiqi Wang<sup>a</sup>, Bangli Xu<sup>a</sup>, Wenyi Huo<sup>b,\*</sup>, Hanchen Feng<sup>a</sup>, Xuefeng Zhou<sup>a</sup>, Feng Fang<sup>a,\*</sup>, Zonghan Xie<sup>c</sup>, Jian Ku Shang<sup>d</sup>, Jianqing Jiang<sup>a,b</sup>

<sup>a</sup> Jiangsu Key Laboratory of Advanced Metallic Materials, Southeast University, Nanjing 211189, China

<sup>b</sup> College of Mechanical and Electrical Engineering, Nanjing Forestry University, Nanjing 210037, China

<sup>c</sup> School of Mechanical Engineering, University of Adelaide, Adelaide, SA 5005, Australia

<sup>d</sup> University of Illinois at Urbana-Champaign, Urbana, IL 61801, USA

## ARTICLE INFO

### Keywords:

High entropy alloy  
Thin film  
Bifunctional electrocatalyst  
Magnetron sputtering  
Water splitting

## ABSTRACT

The creation of high-performing, robust bifunctional electrocatalysts for both cathodic hydrogen evolution reaction (HER) and anodic oxygen evolution reaction (OER) in water-splitting is crucial for producing emerging hydrogen economy. Here we report a high entropy alloy (HEA) – FeCoNiCuPd – thin film catalyst, which demonstrated excellent alkaline HER and OER performance with ultralow overpotentials as low as 29 mV for HER and 194 mV for OER at a current density of 10 mA cm<sup>-2</sup>. The outstanding catalytic activity for HER was found to originate from the multiple active sites present on the FeCoNiCuPd surface, while for OER it came from the highly functional (FeCoNi)-oxyhydroxide species formed on the film surface. Moreover, the two-electrode electrolyzer made of the FeCoNiCuPd film electrodes required a low cell voltage of 1.52 V to achieve 10 mA cm<sup>-2</sup> in 1.0 M KOH, greatly outperforming commercially available Pt/C||RuO<sub>2</sub> electrodes, while maintaining a notable durability. This work demonstrated the remarkable potential of a HEA thin film in catalyzing water-splitting process.

## 1. Introduction

The rapid depletion of fossil fuels driven by rising global energy demand and consequent environmental degradation have motivated the global efforts to seek sustainable energy sources [1]. Hydrogen is regarded as one of the most promising energy carriers to displace and even replace fossil fuels due to its high gravimetric energy density and zero-carbon emissions [2]. It can be made by a variety of physical and chemical processes [3]. Among them, electrochemical water splitting has received much attention as an effective approach for the large-scale production of hydrogen fuel [4]. The overall water electrolysis process consists of two half-cell reactions: cathodic hydrogen evolution reaction (HER) and anodic oxygen evolution reaction (OER) [5]. To tackle the sluggish kinetics and circumvent complex multi-electron reaction pathways, a bifunctional electrocatalyst that could accelerate the reaction rate while lowering the overpotential is highly desirable [6]. Even more appealing would be the emergence of the bifunctional catalysts made from unconventional routes that could simplify the preparation and assembling processes for ease of scalability and low costs [7].

At present, noble metal-based compounds such as IrO<sub>2</sub>/RuO<sub>2</sub> and Pt are known as the benchmark catalysts for the OER and HER [8,9], respectively. However, their high material costs and insufficient stability have greatly hindered their commercial application [10]. In general, the HER catalysts exhibit excellent performance in acidic media, while the OER catalysts are more favorable in the alkaline environment [11]. Since a majority of commercially available electrolysis cells are alkaline types, the pairing of two incompatible catalysts could reduce overall water splitting efficiency. Pd-based catalysts showed impressive capacity towards HER under alkaline conditions and could be used to enhance the overall water splitting process [12–14], but they suffered from the same shortcomings as other precious metal catalysts. Thus, there is an urgent need to develop high-performing and durable catalysts for both alkaline HER and OER in the water electrolysis.

The alloying method has proven to be effective in tuning electronic structure and regulating adsorption free energy of intermediates developed on the catalyst, thereby accelerating the catalytic process. For example, mixing noble metals with 3d metals (Fe/Co/Ni, etc.) could improve the catalytic activity and decrease the usage of the noble metals

\* Correspondence to: School of Materials Science and Engineering, Southeast University, Jiangning District, Nanjing 211189, China.

E-mail addresses: [wuyhuo@njfu.edu.cn](mailto:wuyhuo@njfu.edu.cn) (W. Huo), [fangfeng@seu.edu.cn](mailto:fangfeng@seu.edu.cn) (F. Fang).

<https://doi.org/10.1016/j.apcatb.2022.121472>

Received 11 February 2022; Received in revised form 22 April 2022; Accepted 1 May 2022

Available online 4 May 2022

0926-3373/© 2022 Elsevier B.V. All rights reserved.

[15–17]. Accordingly, the concept of high entropy alloys (HEAs) has been employed to design bifunctional catalysts. HEAs typically consist of five or more principal elements and exhibit a single-phase solid solution [18]. Previous research has indicated that HEAs, e.g., Core-shell CoNiCuMnAl@C nanoparticles, provide superior catalytic activity over the commercial RuO<sub>2</sub> towards OER [19]. The superiority was mainly attributed to the cocktail effect [20], tunable electronic properties [21], and excellent structural stability [22].

To prepare HEA catalysts, a variety of techniques have been introduced, including carbothermal shock [23], mechanical alloying [24], solvothermal synthesis [25], and fast-moving bed pyrolysis (FMBP) method [26]. However, the synthesis of nano-sized HEA-based catalysts is still a challenge, as it often involves complex processes and hyperthermal sintering conditions [27]. In addition, catalyst nanoparticles have to be fixated upon the carriers by a polymeric binder, which lowers conductivity, shields active sites, and hinders mass transport [28].

In this work, a FeCoNiCuPd thin film with a single face-centered cubic (FCC) structure was deposited on carbon fibre cloth (CFC) by magnetron sputtering. The newly-developed HEA/CFC system exhibited superior HER and OER activities compared to the commercially available catalysts under alkaline conditions, resulting in an outstanding water electrolysis performance. By combining the comparative experiments with density functional theory (DFT) calculations, the mechanistic origins for the high bifunctional catalytic efficiency were revealed. Furthermore, the new electrocatalyst showed impressive stability under high current conditions for dozens of hours, outperforming the current commercial systems.

## 2. Experimental

### 2.1. Deposition of FeCoNiCuPd and reference alloy films on carbon fibre cloth

FeCoNiCuPd HEA thin films were deposited on carbon fibre cloth by pulsed DC reactive magnetron sputtering of Fe/Co/Ni/Cu targets (99.99% purity) and Pd particles target (99.99% purity) at 100 W. A pulse DC power controller with 100 kHz pulse frequency, 200  $\mu$ s pulse-on time, and 80% duty cycle was employed for deposition. Prior to deposition, the targets were cleaned by Ar<sup>+</sup> bombardment for 10 min to remove surface impurities. The base pressure of the chamber was kept at  $5.0 \times 10^{-4}$  Pa while the working pressure was set at 0.5 Pa. Pure Ar gas (99.99% purity) was used as sputtering gas with a volumetric flow rate of 30 sccm. The distance between the targets and substrate was set at 150 mm. For comparison purposes, FeCoNiCu, FeCoNiPd, FeCoCuPd, CoNiCuPd, and FeNiCuPd thin films were also prepared with the same deposition parameters. The fabrication process of the HEA thin films is illustrated in Fig. 1. The FeCoNiCuPd HEA film was also deposited on the Ni foam substrate to explore the stability for water splitting under extremely high current condition [9].

### 2.2. Preparation of Pt/C and RuO<sub>2</sub> on carbon fibre cloth

Commercial Pt/C and RuO<sub>2</sub> powders were drop-coated and attached

on the carbon fibre cloth, acting as the HER/OER benchmark catalysts. According to previously reported research [4,6], 5 mg of commercial Pt/C and RuO<sub>2</sub> catalyst powders were dispersed in 1 mL Nafion ethanol solution (980  $\mu$ L ethanol and 20  $\mu$ L of 5 wt% Nafion solution), respectively. The obtained suspension was immersed in an ultrasonic bath for 1 h to prepare the homogeneous mixture. Afterward, 100  $\mu$ L of suspension was dropped onto the CFC electrode ( $\sim 1 \times 1$  cm<sup>2</sup>) with a loading mass of about 0.50 mg cm<sup>-2</sup> and dried at room temperature.

### 2.3. Characterization of the HEA thin films

The microstructure and chemical composition of the thin film samples were examined by field emission scanning electron microscope (FESEM) (FEI Sirion) operating at 20 kV, interfaced with energy-dispersive X-ray spectroscopy (EDS). The high-resolution transmission electron microscopy (HRTEM) (Talos F200X transmission electron microscope) was used to resolve the structural details. The crystalline phase of the samples was investigated by a Bruker D8 XRD system, operating at 40 kV and 35 mA and using Cu K $\alpha$  monochromatic radiation. The X-ray photoelectron spectroscopy (XPS) (Kratos Axis Ultra spectrometer with Al K $\alpha$  radiation) was performed to identify the chemical bonds in the samples, for which the peaks were calibrated using adventitious carbon (C 1 s at 284.6 eV). The release and degree of metallic ions during the chronopotentiometry tests were examined by inductively coupled plasma-optical emission spectrometry (ICP-OES) (SPECTROBLUE ICP-OES). *In-situ* Raman spectroscopy (Alpha 300 ACCESS, WITec) with a 50X objective (Leica-Microsystems) was used to monitor the dynamic surficial rearrangement of FeCoNiCuPd sample during the electrochemical activation process. The wavelength of the laser excitation source was 532 nm with a power of  $\sim 0.5$  mW at a grating of 1200 mm<sup>-1</sup>. Each spectrum was produced by 20 consecutive scans and 5 s exposure time per scan, with a resolution of  $\sim 1$  cm<sup>-1</sup>. Raman signals were recorded in-situ at OCP and under different applied potentials spanning from 1.1 to 1.6 V vs RHE.

### 2.4. Electrocatalytic measurements

All the electrochemical measurements were carried out at room temperature using a CHI 660E electrochemical workstation (Shanghai Chenhua Co., Ltd., P.R. China) with a three-electrode configuration. The as-prepared HEA/CFC samples ( $\sim 1 \times 1$  cm<sup>2</sup>) were designated as the working electrode. The reference electrode is Hg/HgO (+0.098 V vs NHE at 25 °C) and the counter electrode is made from carbon rod. An iR-correction (85%) was adopted for the electrochemical tests. The electrochemical measurements were executed in 1 M KOH aqueous solution. Linear sweep voltametric (LSV) and Tafel plots were obtained at a scan rate of 5 mV/s in 1 M KOH electrolyte. Electrochemical impedance spectroscopic analysis (EIS) was conducted in a frequency range of 0.1–100 kHz. The electrochemically active surface area (ECSA) of electrocatalysts was investigated using cyclic voltammetry (CV) measurements within a non-Faradaic region at a scan rate of 20–100 mV/s. The ECSA of the catalysts was calculated by the ratio of  $C_{dl}$  to  $C_s$ , while the double-layer capacitance was derived from the average absolute

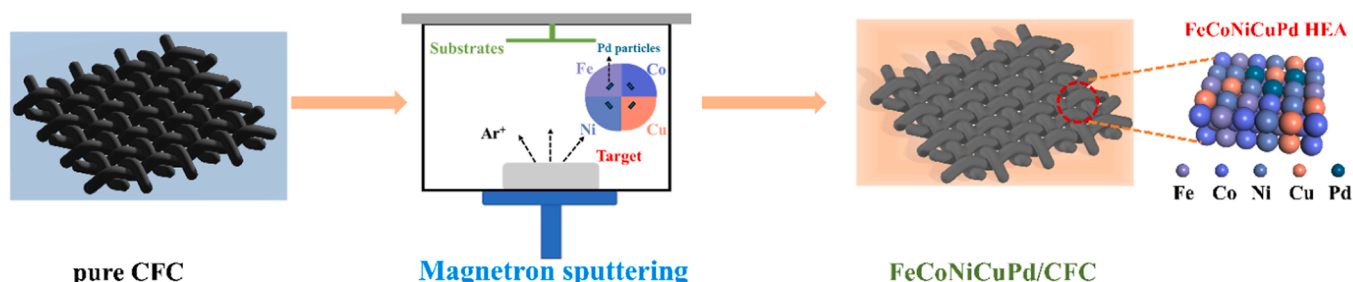


Fig. 1. Schematic illustration of key FeCoNiCuPd thin film fabrication steps.

slope and the general specific capacitance of  $40 \mu\text{F}\cdot\text{cm}^{-2}$  was used. Fourier transformed alternating current voltammetric (FTACV) experiments were performed under a potential amplitude of 100 mV and an AC frequency of 10 Hz by a purpose-built instrument. The chronopotentiometric measurements for the HER and OER were performed at  $-100 \text{ mA cm}^{-2}$  and  $100 \text{ mA cm}^{-2}$  for 36 h, respectively.

## 2.5. Theoretical simulations

DFT simulations were run with the Cambridge Sequential Total Energy Package (CASTEP), one of the main modules in the Materials Studio program [29]. The generalized gradient approximation of Perdew-Burke-Ernzerhof exchange-correlation functionals was adopted for all the calculations [30]. Valence electrons were described by the Kohn-Sham wave functions expanded in a plane wave basis with an energy cutoff set to be 400 eV. The ultrasoft pseudopotentials with the Broyden-Fletcher-Goldfarb-Shannon (BFGS) algorithm were chosen for related ground state geometry optimizations. The reciprocal space was sampled using a  $2 \times 2 \times 1$  Monkhorst-Pack grid. The periodic boundary condition (PBC) was set to maintain a 15 Å vacuum region above the surface to avoid attractions from adjacent periodic mirror images. More details of the model construction and computational methods are presented in the [Supporting Information](#).

## 3. Results

### 3.1. Chemical composition and microstructure analyses

The surface morphologies and chemical composition of as-prepared thin films are shown in Fig. 2a-b and Fig. S1. The HEA films were found to be uniform and smooth with the thickness up to 2 μm. The EDS results (Table. S1 and Fig. S2) demonstrate that the metallic elements are evenly distributed in as-prepared samples. The concentration of Pd is lower than 10 at%, and the contents of other transition metals are close to 23 at%. The FeCoNiCuPd and corresponding quaternary alloys (CoNiCuPd, FeNiCuPd, FeCoNiCu, FeCoNiPd, and FeCoCuPd) (Fig. 2c) exhibit a single face-centered cubic (FCC) structure. The major peaks

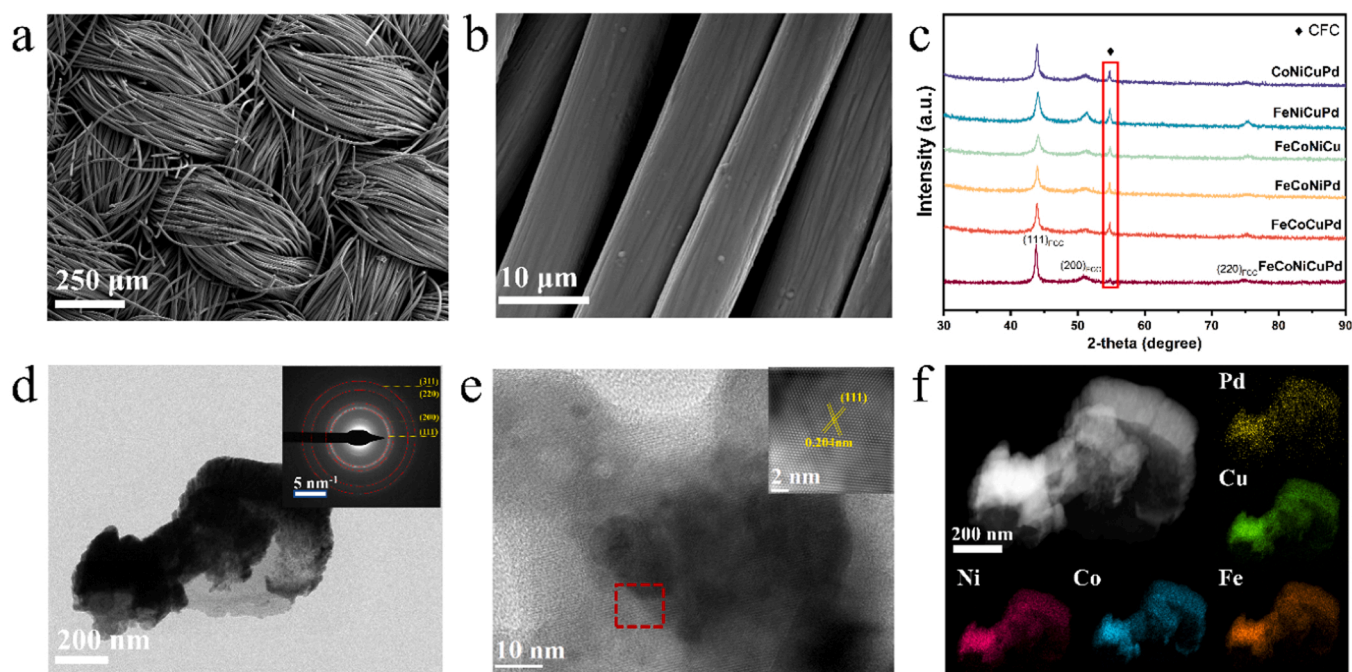
were identified at about  $44^\circ$ ,  $52^\circ$ , and  $77^\circ$ , which can be ascribed to (111), (200), and (220) planes [31], respectively.

Fig. 2d displays the single-phase FCC structure of the as-deposited FeCoNiCuPd alloy film. Fig. 2e shows a lattice fringe of 0.204 nm, corresponding to the (111) plane of the FCC crystals [31]. Combined with the TEM results and the XRD measurements, the FeCoNiCuPd film displays highly crystallized FCC structure. The high-angle annular dark-field (HAADF) and EDS mapping (Fig. 2f) confirm the homogeneous chemical distributions of Fe, Co, Ni, Cu, and Pd elements, consistent with the SEM-EDS results.

To explore the surface chemical bonding states of the samples, X-ray photoelectron spectroscopy (XPS) measurements were carried out. As shown in Fig. 3a, the Fe  $2p_{3/2}$  spectrum could be resolved into two main peaks (metallic  $\text{Fe}^0$  and oxidized  $\text{Fe}^{2+}$ ) along with the satellite peaks. It suggested that the  $\text{Fe}^{2+}$  species was dominant as compared to metallic Fe species, which could be attributed to relatively high chemical activity of Fe and its relatively low redox potential (Table. S2) [32]. However, XPS results (Fig. 3b-e) indicate that Co, Ni, Cu, and Pd elements exist in metallic form. High-resolution  $\text{O}_{1s}$  spectrum could be resolved into two distinctive peaks (Fig. 3f); one can be assigned to M-O bonds and the other is associated with the adsorbed water [33]. Thus, the XPS measurements revealed the metallic bonding nature of the FeCoNiCuPd film with expected surface oxidation.

### 3.2. HER catalytic process

To evaluate the alkaline HER performance of as-synthesized FeCoNiCuPd HEA catalyst, a series of tests and characterizations were carried out in 1 M KOH electrolyte. For comparison purposes, bare CFC, commercial Pt/C catalysts attached on CFC, and quaternary alloy samples were also studied. The HER polarization curves of various catalysts are shown in Fig. 4a. The FeCoNiCuPd catalyst outperformed the quaternary alloy materials and was even superior to the benchmark Pt/C catalyst. The FeCoNiCuPd film electrode required the lowest overpotential (29.7 mV) to achieve the current density of  $10 \text{ mA cm}^{-2}$  (Fig. 4b), which is lower than that of the Pt/C (35.4 mV). The mass activity of the catalysts was also taken into consideration to estimate the



**Fig. 2.** (a-b) SEM image of the FeCoNiCuPd/CFC. (c) XRD spectrums of the FeCoNiCuPd, FeCoCuPd, FeCoNiPd, FeCoNiCu, FeNiCuPd, and CoNiCuPd films on the carbon clothes. (d) TEM images of the FeCoNiCuPd film with the selected area electron diffraction (SAED) pattern (inset). (e) HRTEM image of the FeCoNiCuPd film with the corresponding inverse FFT patterns of the selected zone (inset). (f) HAADF-STEM image and the corresponding EDX elemental maps of FeCoNiCuPd film.



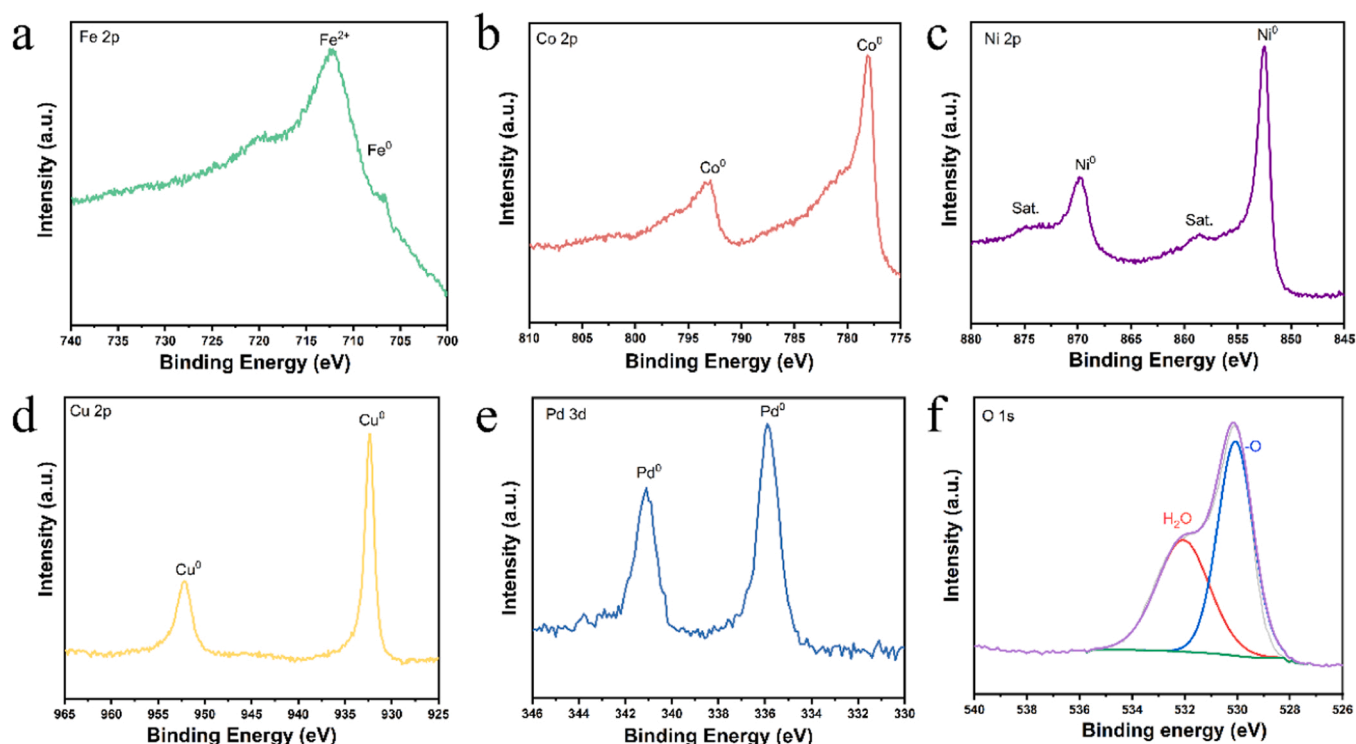


Fig. 3. High-resolution XPS spectra of (a) Fe 2p, (b) Co 2p, (c) Ni 2p, (d) Cu 2p, (e) Pd 2p, and (f) O 1s over FeCoNiCuPd film.

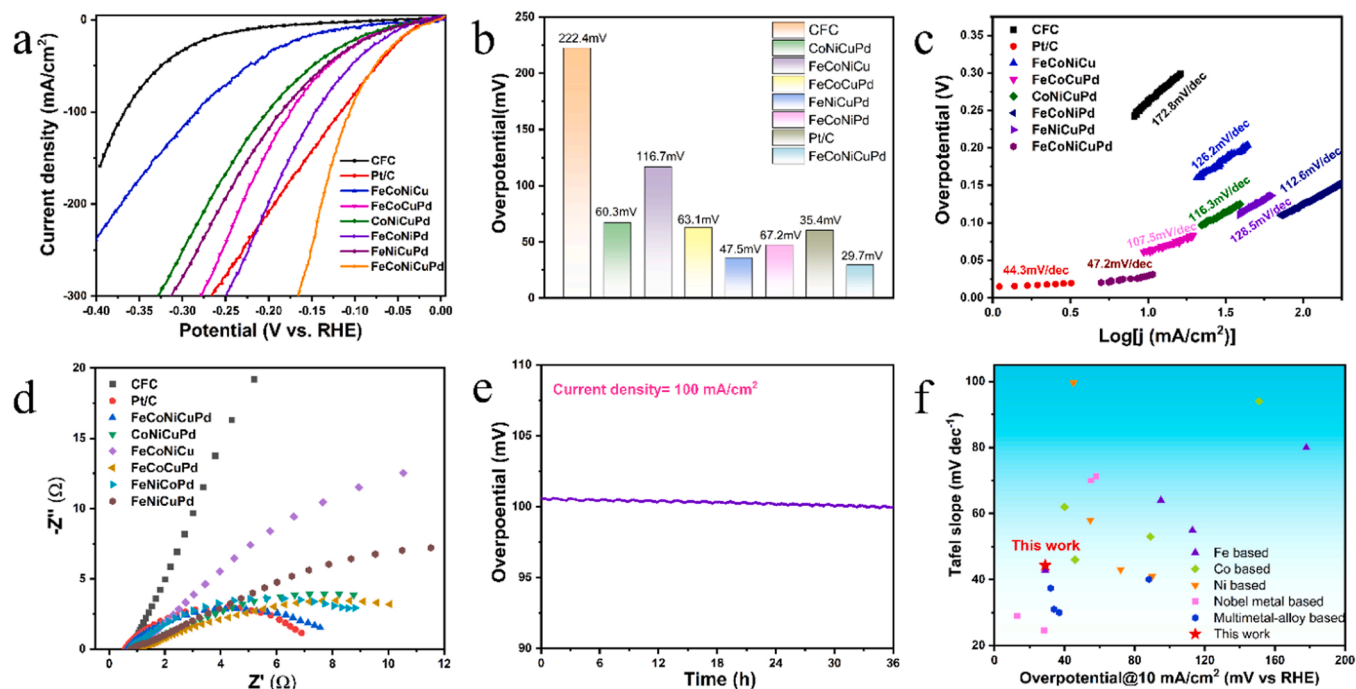


Fig. 4. HER performance evaluation of FeCoNiCuPd in 1 M KOH electrolyte. (a) HER polarization curves. (b) Comparison of overpotential at the  $10 \text{ mA cm}^{-2}$ . (c) Tafel plots derived from HER polarization curves of (a). (d) EIS Nyquist plots. (e) Stability test of FeCoNiCuPd film at  $100 \text{ mA cm}^{-2}$  for 36 h. (f) The comparison in overpotential ( $10 \text{ mA cm}^{-2}$ ) and Tafel slope of our as-prepared FeCoNiCuPd HEA with other reported alkaline HER catalysts (see in Supporting Information).

preparation cost (Fig. S3). The mass current density of the FeCoNiCuPd/CFC electrode at the overpotential of  $100 \text{ mV}$  reached  $\sim 298.53 \text{ A g}^{-1}$ , which is slightly higher than the Pt/C ( $287.85 \text{ A g}^{-1}$ ) but  $\sim 1570$  times greater than the bare CFC ( $0.19 \text{ A g}^{-1}$ ). Considering the high cost of the Pt/C catalyst, the as-prepared catalyst that exhibited a higher electrocatalytic efficiency in this work is promising for HER application.

To probe HER kinetics under alkaline conditions, the Tafel plots of the samples were obtained from the LSV curves. The Tafel slope can be calculated by the Tafel equation [34]:

$$\eta = b * \log j + a$$

where  $\eta$ ,  $b$ , and  $j$  represent the overpotential Tafel plot, and the current



density, respectively. According to Fig. 4c, the FeCoNiCuPd alloy exhibits a low Tafel slope of  $47.2 \text{ mV dec}^{-1}$ , which is comparable to Pt/C ( $44.3 \text{ mV dec}^{-1}$ ) but much lower than those of the quaternary alloys. Therefore, the FeCoNiCuPd alloy showed enhanced HER activity with improved reaction rate. The Tafel slope could also be used to determine the rate-determining step (RDS) during the HER process [35]. In general, the alkaline HER could be divided into two steps [35]: i) Volmer step constituting the water dissociation process; ii) Heyrovsky or Tafel step accounting for the atom combination reaction. For the Heyrovsky step, the  $\text{H}^*$  atom of the catalyst is combined with an electron and  $\text{H}_2\text{O}$  to form a hydrogen molecule (i.e.,  $\text{H}^* + \text{H}_2\text{O} + \text{e}^- \rightarrow \text{H}_2 + \text{OH}^-$ ) [4]. In the Tafel step, two  $\text{H}^*$  atoms are directly bonded and form a hydrogen molecule (i.e.,  $\text{H}^* + \text{H}^* \rightarrow \text{H}_2$ ) [4]. According to the HER kinetics model [36], the theoretical values of Tafel slopes for the Volmer, Heyrovsky, and Tafel reactions were determined to be around 120, 40, and  $30 \text{ mV dec}^{-1}$ , respectively. The HER pathway of the FeCoNiCuPd catalyst was supposed to be governed by the more efficient Volmer-Heyrovsky mechanism for HER, since the related Tafel slope was close to  $40 \text{ mV dec}^{-1}$ , while the other quaternary alloy electrodes were influenced by the Volmer-Tafel mechanism. The enhanced HER kinetics might be ascribed to the increased compositional complexity and the associated synergistic effect, which was supported by Chen's reports [4,11].

In addition, electrochemical impedance spectroscopy (EIS) was performed to probe the interfacial properties and ascertain the electron transfer process [37,38]. The EIS results obtained at an overpotential of 80 mV are shown in Fig. 4d. The charge transfer resistance ( $R_{ct}$ ) of the FeCoNiCuPd catalyst was found to approach that of the Pt/C but was much lower than those of bare CFC and other alloy electrodes. It thus indicated a faster electron transfer that facilitated the HER process at the reaction interfaces.

In addition to the compelling catalytic activity, the electrode durability is crucial for sustaining the HER operation. The long-term HER stability of the FeCoNiCuPd electrode was examined by performing the continuous discharge test at  $-100 \text{ mA cm}^{-2}$  for 36 h in the alkaline electrolyte. As shown in Fig. 4e, the overpotential remained stable throughout the testing period, indicative of the superior durability of FeCoNiCuPd during the HER process. Moreover, the tested electrode did not display any apparent structural change (Fig. S4). SEM images and corresponding EDS mapping also revealed that there was no obvious defects and materials loss occurring on the surface (Fig. S5). According to the ICP (Table. S3) and EDS results (Table. S4), the etching/dissolving of the metal components during the alkaline HER was negligible due to the inherent chemical inertness of the HEA samples [18]. To further elucidate the electrocatalytic performance of the FeCoNiCuPd HEA catalyst in this work, the overpotential required at  $10 \text{ mA cm}^{-2}$  and Tafel plots with different kinds of alkaline HER catalysts were compared, as shown in Fig. 4f and Table S5. The new design produced in this work exhibited superior electrocatalytic activity among its high-performing peers. It was noteworthy that most of previously reported metal-based electrocatalysts were prepared through a wet chemistry method, which promised a large specific surface area and a fine electronic structure for enhanced catalytic performance. However, the practical application and commercialization of those materials are hindered by the problematic loading of powders onto the support substrate, which has limited the production scale, and also caused potential environmental pollution [39]. By contrast, the FeCoNiCuPd film/CFC electrode could be manufactured at an industrial scale while achieving higher alkaline HER activities than most of metal-based electrocatalysts.

### 3.3. OER catalytic activity

The OER performance of various samples was also assessed using a typical three-electrode system under alkaline conditions (i.e., 1 M KOH aqueous solution). As the benchmark catalyst, the commercial  $\text{RuO}_2$  particles were loaded onto the CFC with a mass loading of  $0.50 \text{ mg cm}^{-2}$ . Impressively, the FeCoNiCuPd film/CFC electrode exhibited the best

catalytic response with the ultralow overpotential (194 mV) at  $10 \text{ mA cm}^{-2}$  (Fig. 5a-b). For the control specimens, the overpotentials rose up to 271 mV (FeCoNiCu), 247 mV (FeCoCuPd), 238 mV (CoNiCuPd), 227 mV (FeCoNiPd), and 233 mV (FeNiCuPd), respectively. All of the as-prepared HEA film/CFC electrodes outperformed the commercial  $\text{RuO}_2$  catalyst. Furthermore, the Tafel slope of the FeCoNiCuPd was the lowest ( $39.8 \text{ mV dec}^{-1}$ ) among the tested samples (Fig. 5c), indicative of the fastest OER process. Based on the Butler-Volmer equation [40], the exchange current density of the FeCoNiCuPd film/CFC electrode was determined to be  $3.45 \text{ mA cm}^{-2}$ , higher than those of  $\text{RuO}_2$  ( $1.88 \text{ mA cm}^{-2}$ ) and bare CFC ( $1.27 \text{ mA cm}^{-2}$ ). It suggested that the FeCoNiCuPd alloy displayed faster bonding/charge transferring at the reaction interface [40]. The electrochemical impedance was also measured under the overpotential of 300 mV. As shown in Fig. 5d, the  $R_{ct}$  of the FeCoNiCuPd film was lower than that of  $\text{RuO}_2$ , while the  $R_{ct}$  of bare CFC was too large to be captured in the selected region. It implied the faster charge transfer during the OER process [41], consistent with the Tafel plot results.

To evaluate the exposed active sites, the electrochemical surface area (ECSA) of the film electrodes was determined by measuring double-layer capacitances ( $C_{dl}$ ) [42]. As shown in Figs. S6–7, all of the film electrodes show relatively low values of  $C_{dl}$ , and the ECSAs of those samples were then calculated and found to differ slightly from one another. It might ascribe to the uniform and smooth surface nature of the thin film samples prepared by the magnetron sputtering technique. To verify the inherent OER activity of the catalysts, the specific catalytic performance was estimated (via normalizing the LSV curves by ECSA values). At the overpotential of 300 mV, the FeCoNiCuPd/CFC electrode displayed excellent specific property with a current density of  $5.73 \text{ mA cm}^{-2}_{\text{ECSA}}$ , superior to the other film electrodes (Fig. 5e).

Besides the OER activity, the operational durability of the FeCoNiCuPd film/CFC electrode was evaluated in the alkaline electrolyte (1 M KOH). As shown in Fig. 5f, the performance of the FeCoNiCuPd catalyst exhibited no apparent attenuation during the continuous testing period, with current density maintaining at about  $100 \text{ mA cm}^{-2}$ . According to the ICP (Table. S6) and EDS result (Table. S7), there was negligible etching/dissolution of metallic components during the OER process. SEM images and corresponding EDS mapping also demonstrated that the HEA thin films were mechanically stable without delamination (Fig. S8). In light of these measurements, the excellent stability of the HEA film electrode was achieved. The TEM images of the post-test FeCoNiCuPd film indicated that the surface regions might have undergone the rearrangement as manifested by different contrasts (Fig. S9). As with the commonly used evaluation method for the HER activity, we compared the FeCoNiCuPd catalyst with various kinds of high-performance metal-based OER catalysts (e.g., transition-metal based catalysts, noble-metal based catalysts, and multicomponent alloy-based catalysts). Remarkably, the OER rate of the FeCoNiCuPd alloy outperformed most of the recently reported state-of-the-art OER catalysts (Fig. 5g and Table. S8).

### 3.4. Overall water-splitting performance

In light of the superior catalytic performance of alkaline HER and OER, the FeCoNiCuPd film/CFC electrodes were used as both anode and cathode in the setup of water-alkali electrolyzer with a two-electrode configuration. For comparative purposes, commercial Pt/C and  $\text{RuO}_2$  were also utilized as anode and cathode for overall water splitting. As shown in Fig. 5h, the FeCoNiCuPd film as bifunctional catalyst exhibited excellent catalytic response for overall water splitting, which only required 1.52 V of the cell voltage to achieve a current density of  $10 \text{ mA cm}^{-2}$ . It was substantially lower than that of coupled Pt/C|| $\text{RuO}_2$ . As shown in Fig. S10, the measured voltage at different current densities were slightly larger than the calculated voltages (the sum of HER and OER potentials), which may be caused by the difference in the testing system configuration [8]. The alkaline electrolyzer assembled with the FeCoNiCuPd electrocatalyst displayed outstanding stability at a

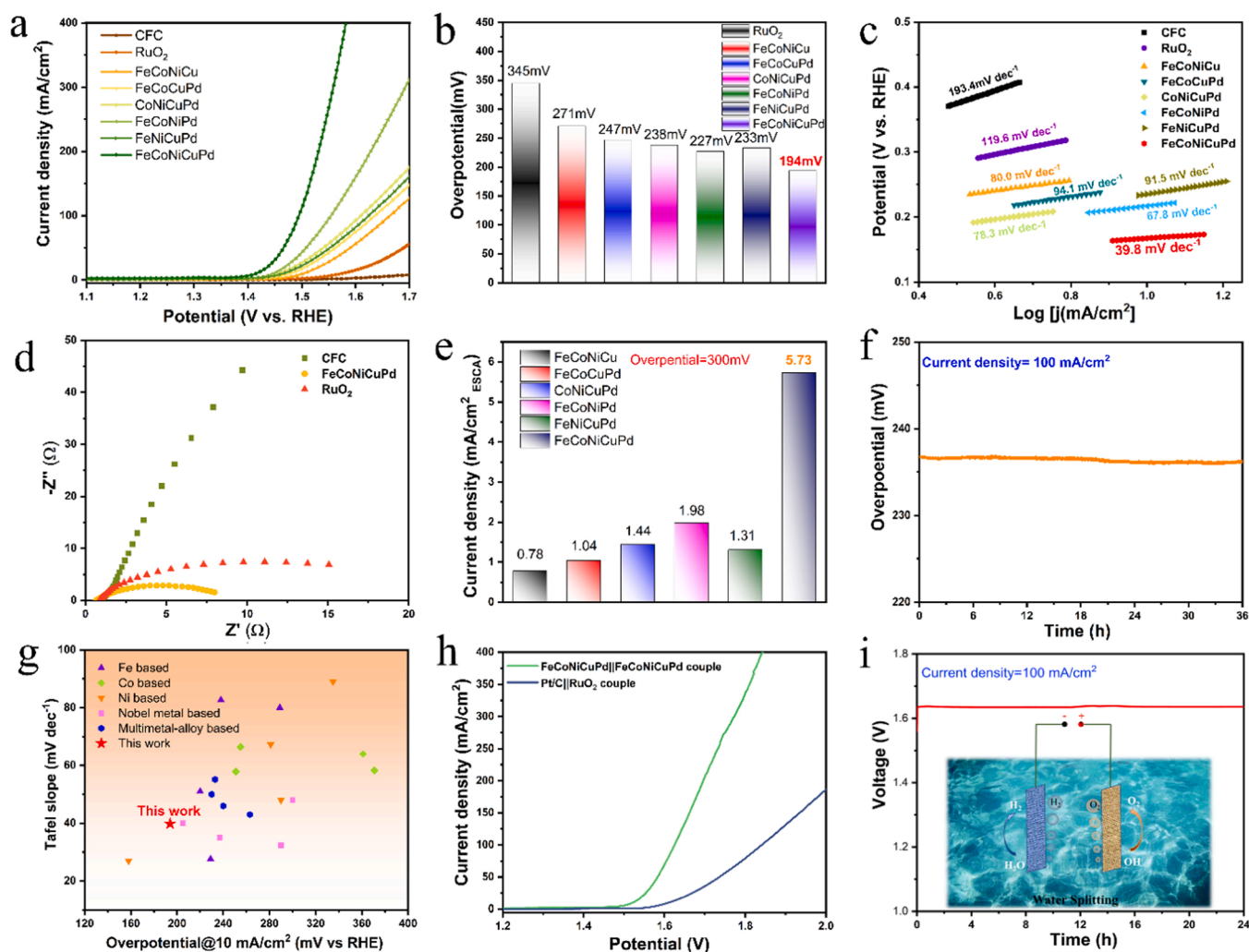


**Fig. 5.** OER performance evaluation of FeCoNiCuPd in 1 M KOH electrolyte. (a) OER polarization curves. (b) Comparison of overpotential at the  $10 \text{ mA cm}^{-2}$ . (c) Tafel plots derived from OER polarization curves of (a). (d) EIS Nyquist plots ( $\eta = 300 \text{ mV}$ ). (e) The specific activity of various catalysts at overpotential of  $300 \text{ mV}$ . (f) Stability test of FeCoNiCuPd film at  $100 \text{ mA cm}^{-2}$  for  $36 \text{ h}$ . (g) The comparison in overpotential ( $10 \text{ mA cm}^{-2}$ ) and Tafel slope of our as-prepared FeCoNiCuPd HEA with other reported alkaline OER catalysts (see in [Supporting Information](#)). (h) Polarization curve of the FeCoNiCuPd || FeCoNiCuPd and Pt/C || RuO<sub>2</sub> electrolyzers in alkaline electrolyte for overall water splitting. (i) Chronopotentiometry curve of the FeCoNiCuPd || FeCoNiCuPd cell at constant current densities of  $100 \text{ mA cm}^{-2}$ .

high current density ( $100 \text{ mA cm}^{-2}$ ) for  $24 \text{ h}$  (Fig. 5i). Moreover, FeCoNiCuPd HEA thin film was also deposited on Ni Foam to prepare the electrolyzer for long-term operation ( $100 \text{ h}$ ) under extremely high current ( $800 \text{ mA cm}^{-2}$ ), which represents a big step forward toward practical applications [9]. The steady chronopotentiometric testing confirmed that the newly-obtained HEA electrodes provided excellent operation stability (Fig. S11a). The SEM, EDS, and XPS results also demonstrated the stable surface morphology and uniform composition distribution after the long-term test (Fig. S11b-h). Multi-step chronopotentiometry tests were also performed in 1 M KOH electrolyte. As shown in Fig. S12, the FeCoNiCuPd/CFC electrode displayed rapid and steady responses, indicative of a potential for more complex operation conditions. Thus, in view of the catalytic activity and durability, the new design produced in this work has shown clear advantages for practical water splitting application.

#### 4. Discussion

To uncover the mechanisms underlying the HER and OER catalytic activities, FTACV experiments, in-situ Raman spectroscopy, and XPS measurements were used in conjunction with DFT calculations. The

detailed analyses and crucial insights were obtained and are given below.

##### 4.1. Key factors controlling the HER catalytic activity

Based on the HER performance of various samples, the FeCoNiCu (yielding the lowest activity) and FeCoNiCuPd (producing the highest activity) were examined to reveal the mechanism underlying the enhanced HER activity. First, the high-order ac harmonic components ( $\geq 4$ ) could circumvent the background charging current and signify the currents of catalytic reactions in FTACV test results [43]. The sixth harmonic FTACV components of the FeCoNiCuPd and reference FeCoNiCu were investigated and compared (Fig. 6a). The FTACV curves of the two samples exhibited no obvious redox peaks, indicating that either the oxidation or reduction, if any, on the metal sites could be negligible. It demonstrated the high stability nature of HEAs in the HER process. Thus, structural models for both FeCoNiCu and FeCoNiCuPd alloys (with the element ratio derived from previous EDS results) were established, as shown in Fig. S13.

Density functional theory (DFT) calculations were carried out to identify the roles of individual metal sites and their synergistic effects.

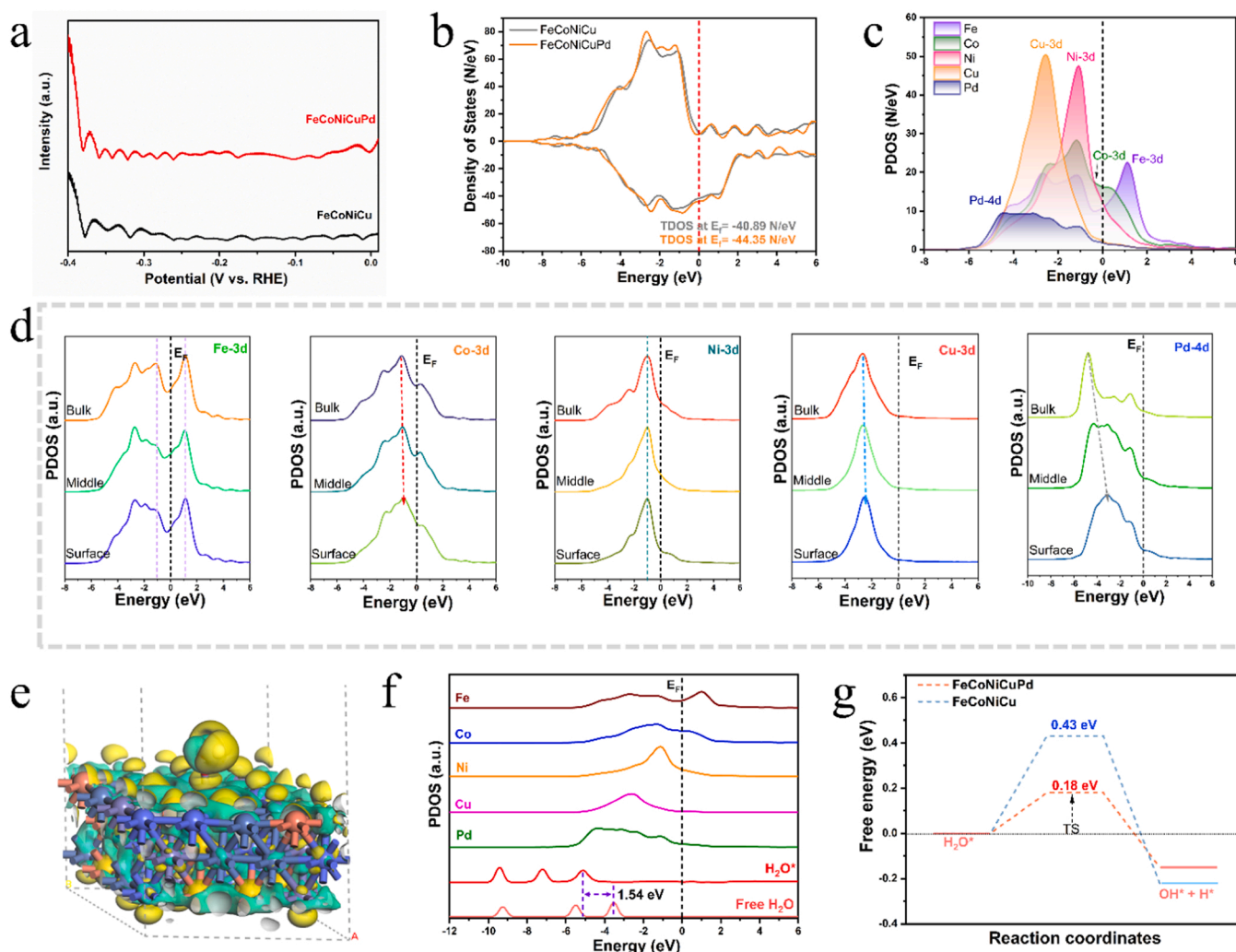


**Fig. 6.** (a) The 6th harmonic FTACV curves of FeCoNiCu and FeCoNiCuPd catalysts. (b) TDOS of FeCoNiCu and FeCoNiCuPd. (c) The PDOSs of the FeCoNiCuPd. (d) The site-dependent PDOSs of Fe, Co, Ni, Cu and Pd in FeCoNiCuPd HEA structure. (e) Charge density difference of H<sub>2</sub>O molecule adsorption on Fe sites over FeCoNiCuPd surface. Yellow and cyan contours represent electrons accumulation and depletion, where the isosurface is set to 0.02 e Å<sup>-3</sup>. (f) The PDOSs for the water adsorption. (g) The calculated activation barriers of water dissociation on FeCoNiCu and FeCoNiCuPd.

For the electrocatalysts, high electrical conductivity was essential for the efficient reaction process. As shown in Fig. 6b, the calculated total density of states of the FeCoNiCu and FeCoNiCuPd alloys were larger than 0 at Fermi level ( $E_F$ ), demonstrating the metallic nature of the HEA samples. The total density of states (TDOS) of FeCoNiCuPd was greater than that of FeCoNiCu, indicative of a higher electron transport rate for HER [44]. Moreover, the projected density of states (PDOSs) of each metal component in the FeCoNiCuPd model was determined to shed light on the electronic structures (Fig. 6c). Pd and Cu sites buried at deeper positions far away the  $E_F$  possessed the electron-rich character and acted as the electron reservoir for HER, as revealed by the electron density difference results (Fig. S14). The broad Fe-3d orbitals exhibited  $e_g$ - $t_{2g}$  splitting with a small barrier, indicative of fast electron transfer. The Ni and Co sites, taking up adjacent positions near  $E_F$ , assisted in the stable adsorption for the vital intermediate ( $H^*$ ) during the alkaline HER process, indicating the high electroactivity [45].

The site-dependent PDOS of individual metal components was also taken into consideration to appreciate their roles for the enhancement of HER activity (Fig. 6d). For Pd sites, moving from the interior to surface positions, the 4d orbitals shifted towards the  $E_F$ , which favored the adsorption of  $H^*$  and further supported the electroactivity [45]. The shifting up towards  $E_F$  also occurred for the electron-rich Cu sites, improving the overall electron transfer among metal sites [46]. Moving

closer to the surface, the Co sites exhibited the decreased  $e_g$ - $t_{2g}$  splitting gap, also enhancing the electron transfer efficiency. Both Fe and Ni sites displayed the site-independent electronic structure from the interior to surface, which may help maintain the stable adsorption of intermediates and initial electroactive feature [46].

Based on the previous work [35], the water dissociation process (the Volmer step) was the first step for alkaline HER, which was usually considered to be the bottleneck of the entire HER process. Here the (111) face was chosen as the main exposed surface for DFT calculations (Fig. S15). The adsorption energy ( $E_{ad}$ ) for water molecules on metal sites was calculated and is shown in Table. S9. Fe sites exhibited the desirable  $E_{ad}$  among all elements, signifying the optimal adsorption of H<sub>2</sub>O. The electron density difference with adsorbed configuration was calculated to verify the boosted adsorption of water molecules. As shown in Fig. 6e, Fe sites presented noticeable electron depletion with the H<sub>2</sub>O adsorption, which attested to the charge transfer during the adsorbing process [24]. Meanwhile, for the reactant H<sub>2</sub>O during the initial adsorption process, the down-shifting of s/p bands also occurred (Fig. 6f), alluding to sufficient electron transfer from the catalyst to water to stabilize adsorbed H<sub>2</sub>O. It is worth noting that the improved capability of water adsorption was in favor of the weakening of O-H bonds in adsorbed H<sub>2</sub>O, thus triggering the subsequent dissociation processes [47]. The adsorption of water dissociation product ( $OH^*$ ) was



also taken into consideration. According to the PDOSs result (Fig. S16), the p-d orbital couplings between the OH\* and Co/Ni sites were observed, which was beneficial for the stable adsorption of OH\*. The  $E_{ad}$  of OH\* was calculated and is summarized in Table. S10. It shows that the produced OH group tended to attach on the Fe-Co/Ni sites, which would facilitate further adsorption of water molecules by the OH group [48]. Finally, due to the multi-active sites and synergistic effect, the FeCoNiCuPd sample displayed an ultralow activation barrier, significantly accelerating the alkaline HER process (Fig. 6g).

With regard to the second step of H\* adsorption/desorption (the Heyrovsky step), the difference in Gibbs free energies ( $\Delta G_{H^*}$ ) can be used as a sensitive indicator [47]. The  $\Delta G_{H^*}$  values for various possible sites on the FeCoNiCuPd (111) planes were calculated (considering computing capability and calculated quantity, the hollow sites were first calculated). According to Fig. 7a, several active sites (e.g., Fe-Ni-Pd, Fe-Co-Pd, Co-Ni-Pd) showed relatively low  $\Delta G_{H^*}$  values (less than 0.25 eV), while the  $\Delta G_{H^*}$  values of other hollow sites were above 0.35 eV. It implied a significant elemental and synergistic effect on hydrogen evolution during the Heyrovsky step. Particularly, the Co-Ni-Pd sites displayed the lowest  $\Delta G_{H^*}$  value (0.12 eV), which were likely to be the optimum sites to advance the all-around reaction. To seek a rational explanation, the d-PDOS of some hollow sites for active adsorption were calculated (Fig. 7b). The results showed that the center of the d-PDOS in Co-Ni-Pd was located at the relatively deep position farther away from  $E_F$ , indicative of the fill of the more antibonding electronic states and consequent weakening of the adsorption of H\* [24]. However, the much deeper d-bands could negatively affect the

adsorption of H\* and indirectly reduce the HER activity. By comparing the  $\Delta G_{H^*}$  values of all the hollow sites, Pd seemed to play a more significant and beneficial role in reducing the energy barrier. Taking Co-Ni-Pd hollow sites as an example, the corresponding bridge sites and top sites were examined to elucidate the underlying mechanism. For the bridging sites, the  $\Delta G_{H^*}$  values were much higher than those of Co-Ni-Pd sites, while both the Co-Pd sites and Ni-Pd sites exhibited smaller values than the Co-Ni sites (Fig. S17). The d-PDOSs of the bridge sites were also calculated (Fig. S18). A similar phenomenon was noticed that the Co-Ni-Pd displayed a preferable d-band center position (not too positive nor negative). The 2D electron density difference over those sites after H\* adsorption was also calculated to investigate the electron transfer capability during the adsorption process. As shown in Fig. 7c, the strong depletion of electrons was noticed around the single Pd sites in Co-Ni-Pd, Co-Pd, and Ni-Pd site configurations, which could enhance electron transfer. The electron accumulation of H\* (blue color) from Co-Ni sites was obviously lower than the former 3 Pd-coordinated sites, suggesting weak electron transfer [24]. On the other hand, the electron accumulation H\* from Co-Ni-Pd sites was the strongest, indicating rapid and efficient electron transfer. In addition, the coordinated atoms (Ni/Co) nearby the Pd atom exhibited evident electron accumulation, indicating that electron transfer from neighboring Pd to adjust their inherent electronic features. These results demonstrated that Pd sites could act as electron reservoirs and enhance the electroactive adsorption of freely migrating H intermediate [46], also in consistent with the PDOSs results.

The bond length for the M-H\* bonds was also an important factor. The bond length of Pd-H\* in Co-Ni-Pd sites (1.876 Å) was greater than

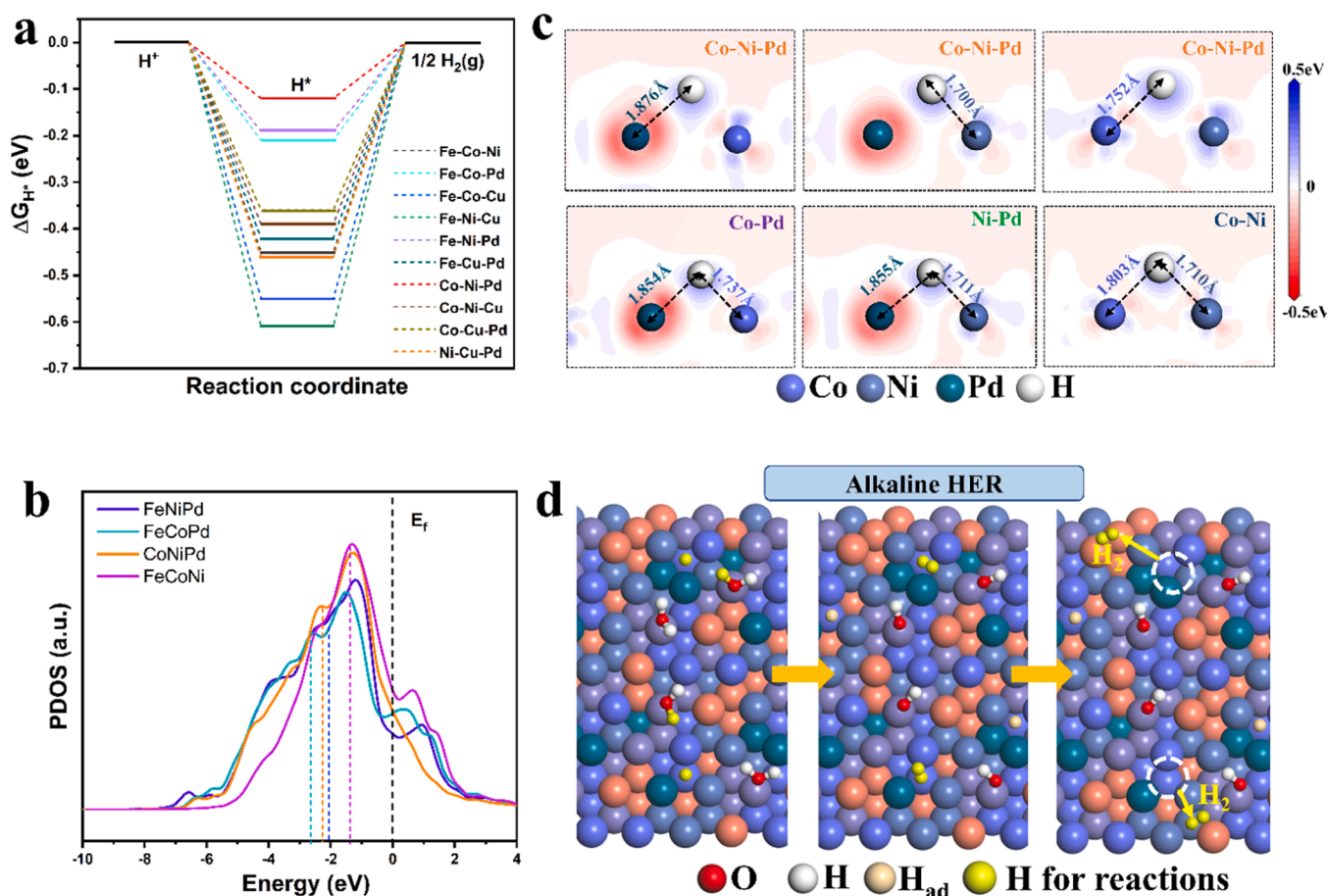


**Fig. 7.** (a) Gibbs free energy ( $\Delta G_{H^*}$ ) profiles of the HER on various catalytic sites at FeCoNiCuPd (111). (b) The d-orbital partial density of states (d-PDOS) of various hollow sites on the FeCoNiCuPd (111) surface. Colored dashed lines highlight the d-band centers of d-PDOS curves. (c) DFT results of electron density differences among various sites after H\* adsorption at (111) surface. Red and blue represent the depletion and accumulation of electrons with the unit of  $e/\text{\AA}^3$ , respectively. (d) Schematic graph of the alkaline HER process over FeCoNiCuPd HEA structure.

those of Co-Pd and Ni-Pd sites, demonstrating a weakening of the electronic interactions [39]. For Co-H\* bonds and Ni-H\* bonds:  $D_{\text{Co-Ni}}(1.803 \text{ \AA}) > D_{\text{Co-Ni-Pd}}(1.752 \text{ \AA}) > D_{\text{Co-Pd}}(1.737 \text{ \AA})$  and  $D_{\text{Ni-Pd}}(1.711 \text{ \AA}) > D_{\text{Co-Ni}}(1.710 \text{ \AA}) > D_{\text{Co-Ni-Pd}}(1.700 \text{ \AA})$ , respectively. Interestingly, the bond length of Co-H\* bonds and Ni-H\* bonds in Co-Ni-Pd sites was medium and smallest. Compared with the previous results, it was found that the adsorption/desorption of H intermediate was affected by the local chemical environment and their synergistic effect rather than single atom sites. It was also supported by the  $\Delta G_{\text{H}^*}$  of single metal sites, which were higher than that of the major bridge and hollow sites (Fig. S17).

Based on the above analysis, the unique mechanism for alkaline electrocatalytic HER was illustrated in Fig. 7d. For the initial process, the Fe sites first adsorbed water molecules to proceed with the Volmer step for water desorption. Owing to the synergistic effect, the hollow sites composed of isolated Pd atoms with other highly active elements (Fe/Co/Ni) presented a low energy barrier to perform the Heyrovsky step with the adsorption and desorption of H intermediate. A detached H product from the HEA surface was then coupled with the H\* in water to accomplish the production of H<sub>2</sub>.

#### 4.2. The mechanism underlying the OER catalytic activity

To reveal the catalytic mechanism for as-prepared FeCoNiCuPd catalyst, the FTACV studies coupled with in-situ Raman spectroscopy

were performed. Similar to the previous measurements, the 6th harmonic FTACV components of CoNiCuPd, FeCoNiCu, FeCoNiPd, FeCoCuPd, FeNiCuPd, FeCoNiCuPd, and CFC at 10 Hz and 100 mV were probed (Fig. 8a). The obtained FTACV results were zoned into three parts, which were related to three kinds of electron transfer step during the electrochemical activation process [49]. Region I and Region II represented the oxidation of various metallic centers and the consequent surficial reconstruction, accompanied by the generation of high-valence metal active sites, respectively [49]. Region III was connected with the fast water splitting and O<sub>2</sub> production with the increasing applied voltage. For the bare CFC, there were no obvious peaks of redox current in the obtained FTACV curve, suggesting that the inner substrates had little effect on further analysis. As for as-prepared film samples, the current signal exhibited apparent rises in the tested potential window (especially in Region II). It might be related to the structural rearrangement toward highly active  $M^{n+/(n+1)+}$  sites during the catalytic reaction. In Region I, the redox current of all samples was much lower than that of Region II. The low current might result from the high abundance of  $M^{2+}$  due to their low redox potential of  $M^{0+}/M^{2+}$  out of the tested range (Table. S1). Compared with the quaternary metallic catalysts, FeCoNiCuPd showed the highest current in Region II, due to sufficient redox of various active metal sites and inherent synergistic effect. In addition, the obtained FTACV result also implied the effect of the single metal active center for surface oxidation. For example, the loss of Ni components (FeCoCuPd) and Pd component (FeCoNiCu) could

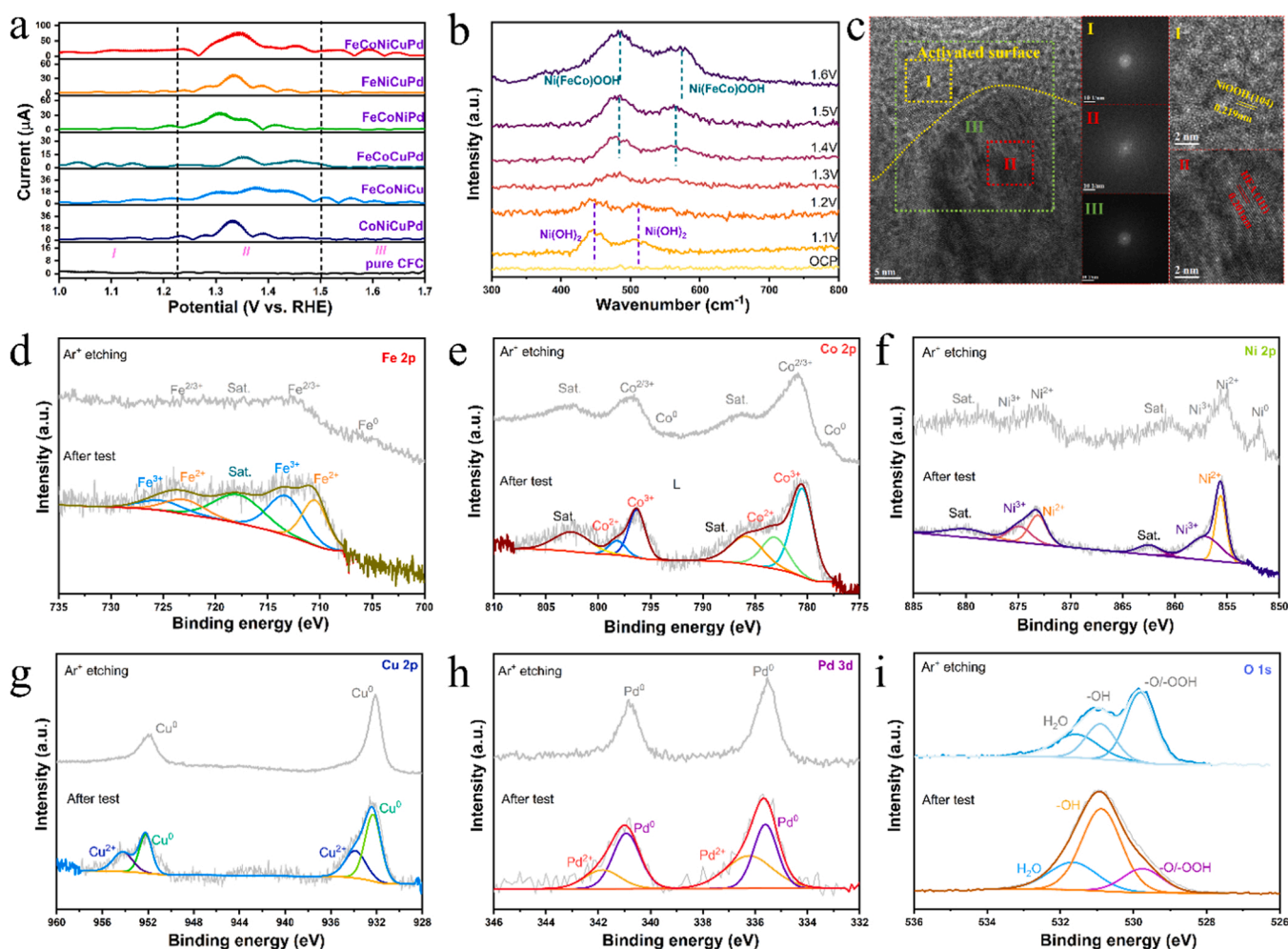


**Fig. 8.** (a) The 6th harmonic FTACV curves of various catalysts. (b) Electrochemical in-situ Raman spectra of FeCoNiCuPd in the range of 300 – 800 cm<sup>-1</sup>. (c) HRTEM image of FeCoNiCuPd catalyst after OER test with corresponding FFT patterns of regions I, II, and III. XPS spectra of tested FeCoNiCuPd sample with further results after Ar<sup>+</sup> plasma etching. (d) Fe 2p, (e) Co 2p, (f) Ni 2p, (g) Cu 2p, (h) Pd 3d, and (i) O 1s, respectively.

obviously reduce redox current and shift the redox peaks towards higher voltage position in Region II, respectively. It manifested the main contribution of Ni sites for the surficial rearrangement and the enhanced charge transfer efficiency by the introduction of Pd composition.

*In-situ* Raman measurement was then performed to monitor the dynamic surface rearrangement of the FeCoNiCuPd sample during the electrochemical activation process. The *in-situ* Raman spectra were collected in alkaline electrolyte from 1.1 V to 1.6 V (vs. RHE) with an interval of 0.1 V. As shown in Fig. 8b, there was no detectable Raman response under open-circuit conditions, indicative of the metallic nature without reconstruction. Under the applied voltage of 1.1 V, two broad peaks (at  $\sim 447\text{ cm}^{-1}/\nu$  ( $\text{Ni}^{\text{II}}\text{-OH}$ ) and at  $512\text{ cm}^{-1}/\nu$  ( $\text{Ni}^{\text{II}}\text{-OH}$ )) emerged in the Raman curve and could be assigned to the  $\text{A}_{1\text{g}}$  stretching modes of  $\text{Ni(OH)}_2$  [50]. With the increasing voltage (from 1.2 V to 1.5 V), the initial peaks gradually disappeared, followed by the growth of a pair of new peaks. The newly generated peaks located at  $482\text{ cm}^{-1}$  ( $\delta$  ( $\text{Ni}^{\text{III}}\text{-O}$ )) and  $566\text{ cm}^{-1}$  ( $\nu$  ( $\text{Ni}^{\text{III}}\text{-O}$ )) were attributed to the  $\text{e}_\text{g}$  bending vibration and the  $\text{A}_{1\text{g}}$  stretching vibration bonds of  $\text{NiOOH}$  [51]. The peaks positioned at  $900\text{--}1150\text{ cm}^{-1}$  emerged under high potential window (Fig. S19), and could be assigned to the vibrational mode of active oxygen intermediates ( $\text{O-O}^{\cdot}$ ) [52]. It was worth noting that two prominent peaks were broadened and right-shifted at 1.6 V. Based on this observation, the following hypothesis was proposed: the fractional structural rearrangements on Fe/Co sites were believed to accompany the OER reaction. It was also supported by the FTACV results (the contributions for the increase of redox current).

Although the surface reconstruction towards highly active metal sites, the XRD patterns after the OER test still maintained original, without new peaks (Fig. S20). It might be ascribed to the small thickness of the newly formed activated surface and low crystallinity of metal (oxy)hydroxide. The corresponding TEM and fast Fourier transform (FFT) images further supported previous perspectives. As shown in Fig. 8c, the surface of FeCoNiCuPd film exhibited obvious reconstruction and heterogeneity after the OER test. The newly produced materials were externally grown on the inner HEA part with small thickness. The HADDF-STEM analysis coupled with EDS mapping also substantiated the existence of the surface oxidative product (Fig. S21). The time-dependent TEM examination further demonstrated the dynamic equilibrium of the surface reconstruction during the OER process without considerably increasing the thickness of the modified surface. However, the thickness of the reconstructed surface layers could gradually thicken with the increasing current density under the intensifying of electrochemical reactions. In addition, HRTEM and FFT studies further revealed the lattice reconstruction of FeCoNiCuPd HEA in detail. Through the electrochemical reactions, the initial lattice fringes transformed into a mixture of Zone I and Zone II with different lattice fringe spacings ( $0.219\text{ nm}$  and  $0.201\text{ nm}$ , respectively). Two regions were assigned to poor crystallinity  $\text{NiOOH}$  (JCPDS No. 06-0075) and highly crystallized HEA, as shown in the FFT images.

The XPS analysis was also provided to elucidate the surface chemical state evolution of FeCoNiCuPd (Fig. 8d-i). After the electrochemical reaction, the Fe, Co, Ni, Cu, Pd, and O spectra were quite different from those of the original sample (Fig. 3). In Fe 2p spectrum, the peak of the pristine metallic component completely disappeared and evolved into  $\text{Fe}^{2+}/\text{Fe}^{3+}$ . As for the high-resolution XPS spectrum of Co 2p and Ni 2p, a similar phenomenon was also found. Notably, the peaks of  $\text{M}^{3+}$  ( $\text{M}=\text{Fe}$ , Co, and Ni) were dominant compared with those of  $\text{M}^{2+}$ , implying that the original metallic centers or  $\text{M}^{2+}$  might efficiently oxidize to a higher valance state during OER. It thus spoke to the previous assumption from the *in-situ* Raman analysis that the Fe/Co/Ni sites were prone to accept the hydroxyls in the alkaline electrolyte under stimulation of potential pulse and form metal (oxy)hydroxides on the surface. The newly generated metal (oxy)hydroxides were believed to enhance the OER catalytic activity [32]. By contrast, the Cu and Pd still exhibited the metallic feature with slight oxidation, indicating that the reconstruction to metal (oxy)hydroxides was selective for the metal sites where Cu/Pd

sites were unable to directly contribute to the structural rearrangement. As for the O 1s spectrum, it was found that the newly emerged peak ( $\text{M-OH}$ ) dominated in the spectrum, attributed to lattice OH species of the hydroxide or (oxy)hydroxide [52]. Meanwhile, the initial pristine M-O peak slightly shifted towards the negative position in the spectrum, relating to the formation of the M-OOH bond [32]. Furthermore, the XPS spectra of the tested sample with  $\text{Ar}^+$  plasma etching was also obtained (Fig. 8d-i, the gray curves). The results suggested that peaks of metallic sites (Fe/Co/Ni) emerged; the peaks of  $\text{Cu}^0/\text{Pd}^0$  completely dominated the XPS spectrum. The M-OH peak intensity decreased, while the M-O peak increased in relation to the O 1s spectrum. It indicated that reconstruction to metal (oxy)hydroxide was a surface engineering process without altering the inner structure, as also supported by the HRTEM results (Fig. 8c).

The FTACV measurements, *in-situ* Raman tests, HRTEM examination, and XPS results collectively shed light on the surface reconstruction of FeCoNiCuPd HEAs towards  $\text{FeCoNiOOH}$  during the OER process. Based on this understanding, the DFT calculation was carried out and focused on the effects of  $\text{FeCoNiOOH}$  on the OER catalysis. To more systematically probe catalytic nature, different oxyhydroxide models of bare  $\text{NiOOH}$ ,  $\text{CoNiOOH}$ ,  $\text{FeNiOOH}$ , and  $\text{FeCoNiOOH}$  were simultaneously built and named  $\text{NiCuPd-R}$ ,  $\text{CoNiCuPd-R}$ ,  $\text{FeNiCuPd-R}$ , and  $\text{FeCoNiCuPd-R}$  (Fig. S22, more details were provided in Supporting Information), respectively. According to the previous research of Nørskov et al. [54], the alkaline OER included four reaction steps with the binding OER intermediates  $\text{*OH}$ ,  $\text{*O}$ , and  $\text{*OOH}$  species on the surface (Fig. 9a). For the electrocatalytic reactions, the conductivity was considered. As shown in Fig. 9b-e, the calculated TDOS at  $E_\text{F}$  of FeCoNiCuPd-R was larger than that of  $\text{NiCuPd-R}$ ,  $\text{FeNiCuPd-R}$ , and  $\text{CoNiCuPd-R}$ , suggesting the improved electron mobility in FeCoNiCuPd-R for fast electron transport.

The Gibbs free energies of four OER steps were calculated concerning various potential metal active sites to examine the energy barriers of adsorption/desorption of key intermediates. As depicted by the calculated results (Fig. 9f), the largest energy barrier ( $\Delta G$ ) of various active sites was quite different. For Ni sites in four models, the third step (formation of  $\text{*OOH}$  from  $\text{*O}$  with  $\text{OH}^-$  in the electrolyte) might be the largest barrier, indicating that this reaction was the RDS on Ni sites for the OER. Fortunately, Ni sites on the FeCoNiCuPd-R model showed a much smaller energy barrier ( $1.48\text{ eV}$ ) than other models, predicting the more superior OER activity of FeCoNiCuPd. As for the Fe sites, the second step acted as the RDS ( $\Delta G_2 = 1.72\text{ eV}$  and  $1.58\text{ eV}$  for  $\text{FeNiCuPd-R}$  and  $\text{FeCoNiCuPd}$ , respectively), which involved the deprotonation of  $\text{*OH}$  to  $\text{*O}$  [53]. Concerning Co sites, the RDS of  $\text{CoNiCuPd-R}$  was Step I (adsorption of OH anion), diverse from the FeCoNiCuPd-R (Step II). The origin of this diversion was attributed to the introduction of Ni sites that reduced the energy barrier of OH adsorption ( $\Delta G_2$ ) from  $1.73\text{ eV}$  to  $1.10\text{ eV}$ , which greatly improved the OER process [55]. Furthermore, with applied potential up to  $1.23\text{ V}$ , thermodynamic overpotentials of all sites were calculated (Fig. 9g). Unsurprisingly, the Ni sites of FeCoNiCuPd-R offered the lowest overpotential ( $0.25\text{ V}$ ) to achieve the exothermic OER catalysis. It showed that the OER reaction on Ni sites of FeCoNiCuPd-R could spontaneously perform the OER catalyzation with an applied potential exceeding  $0.25\text{ V}$ , which all reaction steps were thermodynamically favorable. The other sites (Fe/Co) on FeCoNiCuPd-R also exhibited relatively low energies ( $0.35\text{ eV}/0.32\text{ eV}$ ) to overcome the energy barrier for RDS, as compared with the other samples. It supposedly resulted from the interaction and further synergistic effect of multi-active sites that fine-tuned the adsorption/desorption of OER intermediates. For instance, the  $\text{d-PDOS}$ s of Ni sites could be modulated by the introduction of other metal sites (Fig. 9h). The positions of  $\text{d-band}$  centers could shift towards the  $E_\text{F}$  with the adjustment of Fe/Co, which would in turn affect affinity for OH species (step I) [53]. The coexistence of Fe and Co compositions endowed the optimal location of the  $\text{d-band}$  to provide more appropriate OER active sites, although there might be no exposed Cu/Pd sites on the surface for the reaction. The Cu/Pd sites also



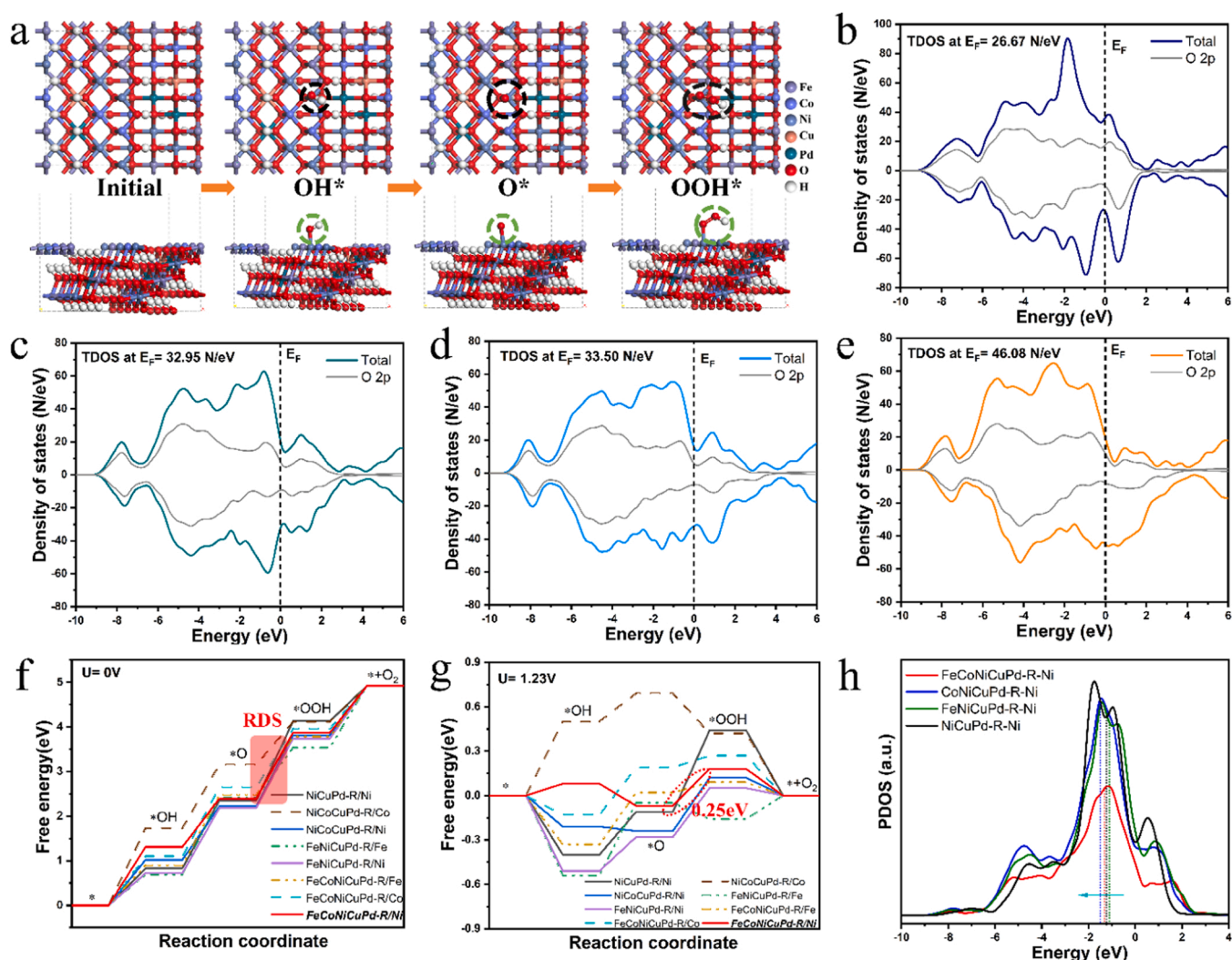


**Fig. 9.** (a) The adsorption geometries of key OER intermediates on the reconstructed FeCoNiCuPd surface during alkaline OER process. TDOS and PDOS of O 2p band for (b) NiCuPd-R, (c) CoNiCuPd-R, (d) FeNiCuPd-R, and (e) FeCoNiCuPd-R, respectively. Calculated  $\rho$ -PDOS of Ni atoms among various structures. Standard free energy diagram of the OER process at (f) 0 V and (g) 1.23 V of various active sites on the different surface-reconstructed samples.

played an indirect role in boosting the OER catalysis, due to their electron-rich nature that accelerates the electron transfer (Fig. S23).

## 5. Conclusions

FeCoNiCuPd thin film was deposited on carbon fibre cloth by magnetron sputtering to serve as bifunctional electrocatalyst for alkaline water splitting. Comparative experiments and DFT calculations revealed that copious active sites and high-entropy cocktail effects are responsible for enhanced alkaline HER activity. The electrochemical measurements showed that the HEA surface underwent a reconstruction that yielded the multicomponent oxyhydroxide. The (FeCoNi)OOH species helped reduce the energy barrier of RDS ( $O^* \rightarrow OOH^*$ ) for OER, thereby accelerating the OER process. The FeCoNiCuPd/CFC assembly showed compelling electrocatalytic capability manifest by a 29 mV overpotential for HER and a 194 mV overpotential for OER at a current density of  $10 \text{ mA cm}^{-2}$ , which is superior to commercially available Pt/C and  $\text{RuO}_2$ . Furthermore, the new electrocatalyst also exhibited impressive HER/OER stability under high current density conditions over long testing hours. This work provides a viable approach to producing high-performing HEA catalysts for water-splitting application.

## CRediT authorship contribution statement

**Shiqi Wang:** Executor of the experiment; Writing – review & editing. **Banli Xu:** Executor of the experiment. **Wenyi Huo:** Analysis of research results. **Hanchen Feng:** Investigation of microstructure. **Xuefeng Zhou:** Analysis of research results. **Feng Fang:** Designer of the experiment; Editing; Supervision. **Zonghan Xie:** Writing – review & editing. **Jianku Shang:** Writing – review & editing. **Jianqing Jiang:** Writing – review & editing.

## Declaration of Competing Interest

The authors declare that they have no known competing financial interests or personal relationships that could have appeared to influence the work reported in this paper.

## Acknowledgements

This work was supported by the National Natural Science Foundation of PR China (No. 52171110) and Jiangsu Key Laboratory of Advanced Metallic Materials, Southeast University, PR China (No. AMM2020A02), and partly supported by Natural Science Foundation of the Jiangsu Higher Education Institutions of China (No. 21KJB430014). The authors

thank Dr. Xiaorong Wang of Liaoning Shihua University, PR China for the assistance with the DFT calculations. The authors acknowledge the computational resources provided by the Big Data Center of Southeast University, PR China.

## Appendix A. Supporting information

Supplementary data associated with this article can be found in the online version at [doi:10.1016/j.apcatb.2022.121472](https://doi.org/10.1016/j.apcatb.2022.121472).

## References

- [1] Y. Feng, Z. Li, C.Q. Cheng, W.J. Kang, J. Mao, G.R. Shen, J. Yang, C.K. Dong, H. Liu, X.W. Du, Strawberry-like  $\text{Co}_3\text{O}_4$ -Ag bifunctional catalyst for overall water splitting, *Appl. Catal. B* 299 (2021), 120658, <https://doi.org/10.1016/j.apcatb.2021.120658>.
- [2] L.G. He, P.Y. Cheng, C.C. Cheng, C.L. Huang, C.T. Hsieh, S. Y. L. (NixFe<sub>2</sub>Co<sub>6</sub>-x-y) Mo<sub>6</sub>C cuboids as outstanding bifunctional electrocatalysts for overall water splitting, *Appl. Catal. B* 290 (2021), 120049, <https://doi.org/10.1016/j.apcatb.2021.120049>.
- [3] Z.Y. Yu, Y. Duan, X.Y. Feng, X.X. Yu, M.R. Gao, S.H. Yu, Clean and affordable hydrogen fuel from alkaline water splitting: Past, recent progress, and future prospects, *Adv. Mater.* 33 (2021) 2007100, <https://doi.org/10.1002/adma.202007100>.
- [4] B. Geng, F. Yan, X. Zhang, Y.Q. He, C.L. Zhu, S.L. Chou, X.L. Zhang, Y.J. Chen, Conductive CuCo-based bimetal organic framework for efficient hydrogen evolution, *Adv. Mater.* 33 (2021) 2106781, <https://doi.org/10.1002/adma.202106781>.
- [5] D.T. Tran, V.H. Hoa, S. Prabhakaran, D.H. Kim, N.H. Kim, J.H. Lee, Activated CuNi@Ni Core@shell structures via oxygen and nitrogen dual coordination assembled on 3D CNTs-graphene hybrid for high-performance water splitting, *Appl. Catal. B* 294 (2021), 120263, <https://doi.org/10.1016/j.apcatb.2021.120263>.
- [6] C.L. Zhu, Z.X. Yin, W.H. Lai, Y. Sun, L.N. Liu, X.T. Zhang, Y.J. Chen, S.L. Chou, Fe-Ni-Mo nitride porous nanotubes for full water splitting and Zn-Air batteries, *Adv. Energy Mater.* 8 (2018) 1802327, <https://doi.org/10.1002/aenm.201802327>.
- [7] J. Luo, J.H. Im, M.T. Mayer, M. Schreier, M.K. Nazeeruddin, N.G. Park, S.D. Tilley, H.J. Fan, M. Grätzel, Water photolysis at 12.3% efficiency via perovskite photovoltaics and Earth-abundant catalysts, *Science* 345 (2014) 1593–1596, <https://doi.org/10.1126/science.1258307>.
- [8] J.H. Lin, P.C. Wang, H.H. Wang, C. Li, X.Q. Si, J.L. Qi, J. Cao, Z.X. Zhong, W.D. Fei, J.C. Feng, Defect-rich heterogeneous MoS<sub>2</sub>/NiS<sub>2</sub> nanosheets electrocatalysts for efficient overall water splitting, *Adv. Sci.* 6 (2019) 1900246, <https://doi.org/10.1002/advs.201900246>.
- [9] F. Yu, H.Q. Zhou, Y.F. Huang, J.Y. Sun, F. Qin, J.M. Bao, W.A. Goddard III, S. Chen, Z.F. Ren, High-performance bifunctional porous non-noble metal phosphide catalyst for overall water splitting, *Nat. Commun.* 9 (2018) 2551, <https://doi.org/10.1038/s41467-018-04746-z>.
- [10] D. Chen, Z.H. Pu, R.H. Lu, P.X. Ji, P.Y. Wang, J.W. Zhu, C. Lin, H.W. Li, X.G. Zhou, Z.Y. Hu, F.J. Xia, J.S. Wu, S.C. Mu, Ultralow Ru loading transition metal phosphides as high-efficient bifunctional electrocatalyst for a solar-to-hydrogen generation system, *Adv. Energy Mater.* 10 (2020) 2000814, <https://doi.org/10.1002/aenm.202000814>.
- [11] X. Zhang, F. Yan, X.Z. Ma, C.L. Zhu, Y. Wang, Y. Xie, S.L. Chou, Y.J. Huang, Y. J. Chen, Regulation of morphology and electronic structure of FeCoNi layered double hydroxides for highly active and stable water oxidation catalysts, *Adv. Energy Mater.* 11 (2021) 2102141, <https://doi.org/10.1002/aenm.202102141>.
- [12] H.B. Liao, C. Wei, J.X. Wang, A. Fisher, T. Sriharan, Z.X. Feng, Z.C. Xu, A multisite strategy for enhancing the Hydrogen Evolution Reaction on a Zn-Pd surface in alkaline media, *Adv. Energy Mater.* 7 (2017) 1701129, <https://doi.org/10.1002/aenm.201701129>.
- [13] L. Li, Y.J. Ji, X.L. Luo, S.Z. Geng, M.M. Fang, Y.C. Pi, Y.Y. Li, X.Q. Huang, Q. Shao, Compressive strain in N-doped palladium/amorphous-cobalt (ii) interface facilitates alkaline Hydrogen Evolution, *Small* 17 (2021) 2103798, <https://doi.org/10.1002/smll.202103798>.
- [14] H. Zhang, Q.F. Jiang, J.H.L. Hadden, F. Xie, D.J. Riley, Pd ion-exchange and ammonia etching of a Prussian Blue analogue to produce a high-performance water-splitting catalyst, *Adv. Funct. Mater.* 31 (2021) 2008989, <https://doi.org/10.1002/adfm.202008989>.
- [15] J. Li, P.P. Zhou, F. Li, R. Ren, Y. Liu, J.R. Niu, J.X. Ma, X.Y. Zhang, M. Tian, J. Jin, J.T. Ma, Ni@Pd/PEI-rGO stack structures with controllable Pd shell thickness as advanced electrodes for efficient hydrogen evolution, *J. Mater. Chem. A* 3 (2015) 11261–11268, <https://doi.org/10.1039/C5TA01805F>.
- [16] Y.L. Xiao, H. Yang, X. Gong, L. Hu, Y.X. Tong, J.Y. Zhang, Electrochemical activation of heterometallic nanofibers for hydrogen evolution, *ACS Appl. Nano Mater.* 3 (2020) 2393–2401, <https://doi.org/10.1021/acsnm.9b02530>.
- [17] R.R. Zhang, Z.T. Sun, R.L. Feng, Z.Y. Lin, H.Z. Liu, M.S. Li, Y. Yang, R.H. Shi, W. H. Zhang, Q.W. Chen, Rapid adsorption enables interface engineering of PdMnCo alloy/nitrogen-doped carbon as highly efficient electrocatalysts for hydrogen evolution reaction, *ACS Appl. Mater. Interfaces* 9 (2017) 38419–38427, <https://doi.org/10.1021/acsami.7b10016>.
- [18] W.Y. Huo, S.Q. Wang, W.H. Zhu, Z.L. Zhang, F. Fang, Z.H. Xie, J.Q. Jiang, Recent progress on high-entropy materials for electrocatalytic water splitting applications, *Tungsten* 3 (2021) 161–180, <https://doi.org/10.1007/s42864-021-00084-8>.
- [19] S.Q. Wang, W.Y. Huo, F. Fang, Z.H. Xie, J.K. Shang, J.Q. Jiang, High entropy alloy/C nanoparticles derived from polymetallic MOF as promising electrocatalysts for alkaline oxygen evolution reaction, *Chem. Eng. J.* 429 (2022), 132410, <https://doi.org/10.1016/j.cej.2021.132410>.
- [20] C.H. Zhan, Y. Xu, L.Z. Bu, H.Z. Zhu, Y.G. Feng, T. Yang, Y. Zhang, Z.Q. Yang, B. L. Huang, Q. Shao, X.Q. Huang, Subnanometer high-entropy alloy nanowires enable remarkable hydrogen oxidation catalysis, *Nat. Commun.* 12 (2021) 6261, <https://doi.org/10.1038/s41467-021-26425-2>.
- [21] D. Zhang, Y. Shi, H. Zhao, W.J. Qi, X.L. Chen, T.R. Zhan, S.X. Li, B. Yang, M.Z. Sun, J.P. Lai, B.L. Huang, L. Wang, The facile oil-phase synthesis of a multi-site synergistic high-entropy alloy to promote the alkaline hydrogen evolution reaction, *J. Mater. Chem. A* 9 (2021) 889–893, <https://doi.org/10.1039/D0TA10574K>.
- [22] X.J. Chang, M.Q. Zeng, K.L. Liu, L. Fu, Phase engineering of high-entropy alloys, *Adv. Mater.* 32 (2020) 1907226, <https://doi.org/10.1002/adma.201907226>.
- [23] Y.G. Yao, Z.N. Huang, P.F. Xie, S.D. Lacey, R.J. Jacob, H. Xie, F.J. Chen, A.M. Nie, T.C. Pu, M. Rehwaldt, D.W. Yu, M.R. Zachariah, C. Wang, R. Shahbazian-Yassar, J. Li, L.B. Hu, Carbothermal shock synthesis of high-entropy-alloy nanoparticles, *Science* 359 (2018) 1489–1494, <https://doi.org/10.1126/science.aan5412>.
- [24] Z.Y. Lv, X.J. Liu, B. Jia, H. Wang, Y. Wu, Z.P. Lu, Development of a novel high-entropy alloy with eminent efficiency of degrading azo dye solutions, *Sci. Rep.* 6 (2016) 34213, <https://doi.org/10.1038/srep34213>.
- [25] M. Bondesgaard, N.L.N. Broge, A. Mamakhel, M. Bremholm, B.B. Iversen, General solvothermal synthesis method for complete solubility range bimetallic and high-entropy alloy nanocatalysts, *Adv. Funct. Mater.* 29 (2019) 1905933, <https://doi.org/10.1002/adfm.201905933>.
- [26] S.J. Gao, S.Y. Hao, Z.N. Huang, Y.F. Yuan, S. Han, L.C. Lei, X.W. Zhang, R. Shahbazian-Yassar, J. Lu, Synthesis of high-entropy alloy nanoparticles on supports by the fast moving bed pyrolysis, *Nat. Commun.* 11 (2020) 2016, <https://doi.org/10.1038/s41467-020-15934-1>.
- [27] K. Li, W. Chen, Recent progress in high-entropy alloys for catalysts: synthesis, applications, and prospects, *Mater. Today Energy* 20 (2021), 100638, <https://doi.org/10.1016/j.mtener.2021.100638>.
- [28] H.M. Sun, Z.H. Yan, F.M. Liu, W.C. Xu, F.Y. Cheng, J. Chen, Self-supported transition-metal-based electrocatalysts for hydrogen and oxygen evolution, *Adv. Mater.* 32 (2020) 1806326, <https://doi.org/10.1002/adma.201806326>.
- [29] S.J. Clark, M.D. Segall, C.J. Pickard, P.J. Hasnip, M.J. Probert, K. Refson, M. C. Payne, First principles methods using CASTEP, *Z. Krist.* 220 (2005) 5–6, <https://doi.org/10.1524/zkri.220.5.567.65075>.
- [30] J.P. Perdew, K. Burke, M. Ernzerhof, Generalized gradient approximation made simple, *Phys. Rev. Lett.* 77 (1996) 3865–3868, <https://doi.org/10.1103/PhysRevLett.77.3865>.
- [31] N.K. Katiyar, S. Dhakar, A. Parui, P. Gakhad, A.K. Singh, K. Biswas, C.S. Tiwary, S. Sharma, Electrooxidation of hydrazine utilizing high-entropy alloys: assisting the oxygen evolution reaction at the thermodynamic voltage, *ACS Catal.* 11 (2021) 14000–14007, <https://doi.org/10.1021/acscatal.1c03571>.
- [32] N. Zhang, X.B. Feng, D.W. Rao, X. Deng, L.J. Cai, B.C. Qiu, R. Long, Y.J. Xiong, Y. Lu, Y. Chai, Lattice oxygen activation enabled by high-valence metal sites for enhanced water oxidation, *Nat. Commun.* 11 (2020) 4066, <https://doi.org/10.1038/s41467-020-17934-7>.
- [33] H.M. Zhang, Y. Lv, C. Chen, C.W. Lv, X.Y. Wu, J.X. Guo, D.Z. Jia, Inter-doped ruthenium-nickel oxide heterostructure nanosheets with dual active centers for electrochemical/solar-driven overall water splitting, *Appl. Catal. B* 298 (2021), 120611, <https://doi.org/10.1016/j.apcatb.2021.120611>.
- [34] X. Luo, P.X. Ji, P.Y. Wang, R.L. Cheng, D. Chen, C. Lin, J.N. Zhang, J.W. He, Z. H. Shi, N. Li, S.Q. Xiao, S.C. Mu, Interface engineering of hierarchical branched Mo-doped Ni<sub>3</sub>S<sub>2</sub>/Ni<sub>3</sub>P<sub>2</sub> hollow heterostructure nanorods for efficient overall water splitting, *Adv. Energy Mater.* 10 (2020) 1903891, <https://doi.org/10.1002/aenm.201903891>.
- [35] C.Z. Wang, X.D. Shao, J. Pan, J.G. Hu, X.Y. Xu, Redox bifunctional activities with optical gain of Ni<sub>3</sub>S<sub>2</sub> nanosheets edged with MoS<sub>2</sub> for overall water splitting, *Appl. Catal. B* 268 (2020), 118435, <https://doi.org/10.1016/j.apcatb.2019.118435>.
- [36] Y. Yang, K. Zhang, H. Lin, X. Li, H.C. Chan, L. Yang, Q. Gao, MoS<sub>2</sub>-Ni<sub>3</sub>S<sub>2</sub> heteronanorods as efficient and stable bifunctional electrocatalysts for overall water splitting, *ACS Catal.* 7 (2017) 2357–2366, <https://doi.org/10.1021/acscatal.6b03192>.
- [37] E.L. Fernández, J. Gil-Rostra, J.P. Espinós, A.R. González-Elipe, A. de Lucas Consuegra, F. Yubero, Chemistry and electrocatalytic activity of nanostructured nickel electrodes for water electrolysis, *ACS Catal.* 10 (2020) 6159–6170, <https://doi.org/10.1021/acscatal.0c00856>.
- [38] S.L. Zhu, Y.Y. Zhou, Y.Q. Liang, Z.Y. Li, S.L. Wu, Z.D. Cui, S.Y. Luo, Enhanced electrocatalysis for hydrogen evolution over a nanoporous NiAlTi/Al<sub>3</sub>Ti hybrid, *ACS Appl. Energy Mater.* 4 (2021) 7579–7588, <https://doi.org/10.1021/acsaem.1c00854>.
- [39] Z. Jia, K. Nomoto, Q. Wang, C. Kong, L.G. Sun, L.C. Zhang, S.X. Liang, Jian Lu, J. J. Kruzic, A self-supported high-entropy metallic glass with a nanosponge architecture for efficient hydrogen evolution under alkaline and acidic conditions, *Adv. Funct. Mater.* 31 (2021) 2101586, <https://doi.org/10.1002/adfm.202101586>.
- [40] N.T. Suen, S.F. Hung, Q. Quan, N. Zhang, Y.J. Xu, H.M. Chen, Electrocatalysis for the oxygen evolution reaction: recent development and future perspectives, *Chem. Soc. Rev.* 45 (2017) 337–365, <https://doi.org/10.1039/C6CS00328A>.

- [41] N. Li, R.G. Hadt, D. Hayes, L.X. Chen, D.G. Nocera, Detection of high-valent iron species in alloyed oxidic cobaltates for catalysing the oxygen evolution reaction, *Nat. Commun.* 12 (2021) 4218, <https://doi.org/10.1038/s41467-021-24453-6>.
- [42] N. Li, H. Tan, X. Ding, H.L. Duan, W. Hu, G.N. Li, Q.Q. Ji, Y. Lu, Y. Wang, F.C. Hu, C. Wang, W.R. Cheng, Z.H. Sun, W.S. Yan, Phase-mediated robust interfacial electron-coupling over core-shell Co@ carbon towards superior overall water splitting, *Appl. Catal. B* 266 (2020), 118621, <https://doi.org/10.1016/j.apcatb.2020.118621>.
- [43] S.A. Bonke, A.M. Bond, L. Spiccia, A.N. Simonov, Parameterization of water electrooxidation catalyzed by metal oxides using fourier transformed alternating current voltammetry, *J. Am. Chem. Soc.* 138 (2016) 16095–16104, <https://doi.org/10.1021/jacs.6b10304>.
- [44] Y. Liu, C. Ma, Q. Zhang, W. Wang, P. Pan, L. Gu, D. Xu, J. Bao, Z. Dai, 2D electron gas and oxygen vacancy induced high oxygen evolution performances for advanced Co<sub>3</sub>O<sub>4</sub>/CeO<sub>2</sub> nanohybrids, *Adv. Mater.* 31 (2019) 1900062, <https://doi.org/10.1002/adma.201900062>.
- [45] J. Jin, J. Yin, H.B. Liu, B.L. Huang, Y. Hu, H. Zhang, M.Z. Sun, Y. Peng, P.X. Xi, C. H. Yan, Atomic sulfur filling oxygen vacancies optimizes h absorption and boosts the Hydrogen Evolution Reaction in alkaline media, *Angew. Chem. Int. Ed.* 60 (2021) 14117–14123, <https://doi.org/10.1002/anie.202104055>.
- [46] H.D. Li, Y. Han, H. Zhao, W.J. Qi, D. Zhang, Y.D. Yu, W.W. Cai, S.X. Li, J.P. Lai, B. L. Huang, L. Wang, Fast site-to-site electron transfer of high-entropy alloy nanocatalyst driving redox electrocatalysis, *Nat. Commun.* 11 (2020) 5437, <https://doi.org/10.1038/s41467-020-19277-9>.
- [47] X. Zhao, X.Y. Li, D.D. Xiao, M.X. Gong, L.L. An a, P.F. Gao, J.L. Yang, D.L. Wang, Isolated Pd atom anchoring endows cobalt diselenides with regulated water-reduction kinetics for alkaline hydrogen evolution, *Appl. Catal. B* 295 (2021), 120280, <https://doi.org/10.1016/j.apcatb.2021.120280>.
- [48] R.Q. Yao, Y.T. Zhou, H. Shi, W.B. Wan, Q.H. Zhang, L. Gu, Y.F. Zhu, Z. Wen, X. Y. Lang, Q. Jiang, Nanoporous surface high-entropy alloys as highly efficient multisite electrocatalysts for nonacidic hydrogen evolution reaction, *Adv. Funct. Mater.* 31 (2021) 2009613, <https://doi.org/10.1002/adfm.202009613>.
- [49] J.S. Chen, H. Li, Z.X. Yu, C. Liu, Z.W. Yuan, C.J. Wang, S.L. Zhao, G. Henkelman, S. Z. Li, L. Wei, Y. Chen, Octahedral coordinated trivalent cobalt enriched multimetal oxygen-evolution catalysts, *Adv. Energy Mater.* 10 (2020) 2002593, <https://doi.org/10.1002/aenm.202002593>.
- [50] H.B. Li, M.H. Yu, F.X. Wang, P. Liu, Y. Liang, J. Xiao, C.X. Wang, Y.X. Tong, G. W. Yang, Amorphous nickel hydroxide nanospheres with ultrahigh capacitance and energy density as electrochemical pseudocapacitor materials, *Nat. Commun.* 4 (2013) 1894, <https://doi.org/10.1038/ncomms2932>.
- [51] S.L. Li, Z.C. Li, R.G. Ma, C.L. Gao, L.L. Liu, L.P. Hu, J.L. Zhu, T.M. Sun, Y.F. Tang, D. M. Liu, J.C. Wang, A glass-ceramic with accelerated surface reconstruction toward the efficient oxygen evolution reaction, *Angew. Chem. Int. Ed.* 60 (2021) 3773–3780, <https://doi.org/10.1002/anie.202014210>.
- [52] B.J.T. Iewski, O. Diaz-Morales, D.A. Vermaas, A. Longo, W. Bras, M.T.M. Koper, W. A. Smith, In situ observation of active oxygen species in Fe-containing Ni-based oxygen evolution catalysts: The effect of pH on electrochemical activity, *J. Am. Chem. Soc.* 137 (2015) 15112–15121, <https://doi.org/10.1021/jacs.5b06814>.
- [53] J. Dong, Y. Lu, X.X. Tian, F.Q. Zhang, S. Chen, W.J. Yan, H.L. He, Y.S. Wang, Y. B. Zhang, Y. Qin, M.L. Sui, X.M. Zhang, X.J. Fan, Genuine active species generated from fe3n nanotube by synergistic CoNi doping for boosted oxygen evolution catalysis, *Small* 16 (2020) 2003824, <https://doi.org/10.1002/sml.202003824>.
- [54] A. Valdes, Z.W. Qu, G.J. Kroes, J. Rossmeisl, J.K. Nørskov, Oxidation and photo-oxidation of water on TiO<sub>2</sub> surface, *J. Phys. Chem. C* 112 (2008) 9872–9879, <https://doi.org/10.1021/jp711929d>.
- [55] W. Cheng, X. Zhao, H. Su, F. Tang, W. Che, H. Zhang, Q. Liu, Lattice-strained metal–organic-framework arrays for bifunctional oxygen electrocatalysis, *Nat. Energy* 4 (2019) 115–122, <https://doi.org/10.1038/s41560-018-0308-8>.